Breathers and multibreathers in a periodically driven damped discrete nonlinear Schrödinger equation

Michael Kollmann and Hans W. Capel

Institute for Theoretical Physics, University of Amsterdam, Valckenierstraat 65, 1018 XE Amsterdam, The Netherlands

Tassos Bountis

*Department of Mathematics, Center for Research and Applications of Nonlinear Systems, University of Patras,
Patras 26500, Greece*

We study an integrable discretization of the nonlinear Schrödinger equation (NLS) under the effects of damping and periodic driving, from the point of view of spatially localized solutions oscillating in time with the driver's frequency. We locate the equilibrium states of the discretized (DNLS) system in the plane of its dissipation Γ and forcing amplitude H parameters and use a shooting algorithm to construct the desired solutions $\psi_n(t) = \phi_n \exp(it)$ as homoclinic orbits of a four-dimensional symplectic map in the complex ϕ_n, ϕ_{n+1} space, for $-\infty < n < \infty$. We derive, in the $\Gamma = 0$ case, closed form expressions for two fundamental such solutions having a single hump in n, ψ_n^+, and ψ_n^-, and determine analytically their threshold of existence in the (Γ, H) plane using Mel'nikov's theory. Then, we demonstrate numerically that above this threshold a remarkable variety of multihump structures appear, whose complexity in terms of their spatial extrema grows with increasing H. All these solutions are numerically found to be unstable in time, except for ψ_n^-, which is seen to be stable over a certain region in the (Γ, H) plane. In the continuum limit our results are in close agreement with recent studies on the NLS equation. From a more general perspective, we view these DNLS multihump solutions as homoclinic orbits of a higher-dimensional map thereby providing a possible mechanism for explaining the occurrence of similar structures called discrete (multi-) breathers found in a wide variety of one-dimensional nonlinear lattices. [S1063-651X(98)10511-1]

I. INTRODUCTION

Integrable nonlinear evolution equations and their spatially discretized counterparts, integrable nonlinear differential-difference equations, are of great interest in many fields of physics. In fact, their applicability becomes even broader as soon as nonintegrable perturbations are considered. In particular, the sine-Gordon equation and its small amplitude limit, the nonlinear Schrödinger equation (NLS) in the presence of damping and periodic driving have been extensively studied since they are related to such systems as long Josephson junctions, easy-axis ferromagnets, rf-driven plasmas, and nonlinear optics [1–5].

As first realized in an adiabatic inverse scattering approach by Kaup and Newell [6], the periodically driven damped NLS admits two coexisting soliton solutions, if the damping and driving terms are small enough. The lower driving threshold for the existence of these solutions was found to be a linear function of the damping constant. One of these solutions, called the bright soliton, is always unstable in time, whereas the dark soliton is stable for certain combinations of damping and driving.

Recently, Barashenkov and Smirnov [7] extended the existence and stability chart for these NLS solitons to larger parameter values. Moreover, in a subsequent paper [8] it was demonstrated that these single-hump solutions can give rise to multihump structures in certain regions of the parameter plane. The possibility that NLS solitons could form bound states had been predicted earlier using a variational argument [9,10] and adiabatic inverse scattering theory [10,11].

In the present paper we consider a spatially discretized version of the periodically driven damped nonlinear Schrödinger equation (DNLS)

$$i \delta \frac{\partial}{\partial t} \psi_n + \frac{\psi_{n+1} + \psi_{n-1}}{2} (1 + |\psi_n|^2)$$

$$= (1 - i\gamma)\psi_n - h \exp(it), \quad n \in \mathbb{Z} \quad (1)$$

and address the question of how the existence chart of its solitonlike solutions is affected by discretization. By a solitonlike solution of the DNLS we mean any localized solution that is asymptotically flat in the discretized space variable and oscillates periodically in time. In fact, in accordance with recent terminology we shall refer to these solutions as breathers and multibreathers [12,13].

To construct (multi)breathers, we eliminate the time dependence of the DNLS system (1) and write the stationary part of the equations as a four-dimensional (4D) mapping, which we study in Sec. II by means of fixed point analysis and Mel'nikov theory [14–16]. The integrable part of the mapping corresponds to the Ablowitz-Ladik discretized version of the NLS [17].

Flat solutions of the DNLS correspond to fixed points of the map, whereas breather solutions approach a fixed point asymptotically as $|n| \to \infty$. In the language of nonlinear mappings these orbits are called homoclinic or heteroclinic, depending on whether their asymptotic values at $n = -\infty$ and at

$n = \infty$ coincide or not. In this paper we do not consider heteroclinic orbits and formulate the following existence criterion:

A necessary condition for the existence of breather solutions is that the 4D mapping obtained by eliminating the time dependence in Eq. (1) possesses a hyperbolic fixed point equipped with a 2D stable and a 2D unstable manifold. If the intersection of these manifolds is not empty, then the condition is also sufficient.

Using this criterion, we obtain the domain of DNLS breathers in the plane of forcing versus damping parameters. More precisely, in Sec. II A, the upper boundary of this region is derived from a stability analysis of all fixed point of the DNLS. The line defining this boundary coincides, up to scaling, with the line obtained in [7] for the NLS.

The lower boundary is obtained in Sec. II B from the tangential intersection of the invariant manifolds of a hyperbolic fixed point. Using a Mel'nikov approach proposed in [15] we derive a vector whose zeros correspond to transversal intersections of the invariant manifolds. As we have demonstrated in an application of this approach to a system of coupled DNLS equations [16], any Mel'nikov zero is sufficient to approximately construct a homoclinic solution. Tangential intersection of the manifolds yields the lower existence threshold. Thus, we are able to extend the result of Kaup and Newell [6], obtained for the NLS, by providing correction terms that are purely due to the discretization.

In Sec. III, single-hump structures (or breathers) are discussed in some detail. For the undamped case, the ψ^+ and ψ^- solutions are given analytically and are shown to be marginally stable. For finite $\gamma > 0$ we describe these solutions numerically under variation of damping and driving parameters.

In Sec. IV, we employ a shooting algorithm to locate multibreather solutions. Our method exploits the smoothness of the unstable (stable) manifold along the outgoing (incoming) direction. The increasingly complex structure of these solutions can be labeled by the number of extrema of their spatial oscillations. Defining an order parameter by the sum of $|\phi_n|^2$, we vary h and observe certain bifurcation phenomena involving a single solution or pairs of solutions and occurring at turning points of the order parameter.

Finally, in Sec. V, we summarize our results and propose that multibreathers can be explained geometrically in terms of intersections of higher order lobes of the invariant manifolds of an unstable fixed point.

II. THE PERIODICALLY DRIVEN AND DAMPED DNLS

The NLS equation, including effects of damping and periodic driving, is given in continuous time and space variables by the partial differential equation (pde)

$$i\Psi_t + \Psi_{xx} + 2|\Psi|^2\Psi = -i\Gamma\Psi - He^{i\Omega t}. \quad (2)$$

In agreement with [7] we assume that both the damping coefficient Γ and the driving amplitude H are real and positive. (An extra phase factor in H may always be removed by a translation in time.) As was realized in [7,18,19], one of the three parameters Ω, H, Γ can be scaled out using the transformation

$$\tilde{\Psi}(x,t) = k\Psi(kx, k^2 t), \quad \tilde{\Omega} = k^2\Omega, \quad \tilde{\Gamma} = k^2\Gamma, \quad \tilde{H} = k^3 H. \quad (3)$$

which leaves Eq. (2) unchanged. We follow here [7] and fix $\Omega \equiv 1$.

The Ablowitz-Ladik discretized version of the NLS is obtained by replacing the dispersive term and the nonlinear term in Eq. (2) with their symmetric discretizations on an infinite lattice [17]. Denoting by Δ the distance between subsequent lattice points and $\Psi_n = \Psi(n\Delta)$ these terms become

$$\frac{\Psi_{n+1} + \Psi_{n-1} - 2\Psi_n}{\Delta^2} + |\Psi_n|^2(\Psi_{n+1} + \Psi_{n-1}). \quad (4)$$

For the purpose of numerical calculations and comparison with similar results in the literature we work throughout this paper with the lattice spacing $\Delta = \frac{1}{5}$ unless stated otherwise. Expressing now the NLS (2) with (4) in the rescaled quantities

$$\psi_n = \Delta\Psi_n, \quad \delta = \tfrac{1}{2}\Delta^2, \quad \gamma = \tfrac{1}{2}\Delta^2\Gamma, \quad h = \tfrac{1}{2}\Delta^3 H \quad (5)$$

we arrive at the DNLS system (1). With the ansatz $\psi_n(t) = \phi_n e^{it}$ (ϕ_n time independent) we obtain stationary solutions of this system from the map

$$\frac{\phi_{n+1} + \phi_{n-1}}{2}(1 + |\phi_n|^2) = (\mu - i\gamma)\phi_n - h, \quad n \in \mathbb{Z} \quad (6)$$

with $\mu = 1 + \delta$. These solutions may be stable or unstable in time (see Sec. III).

It is useful to remark that the transformations (3) and (5) are by no means equivalent, in spite of their formal similarity. In the first transformation the driving frequency is eliminated by rescaling all time and space parameters. In the second, the DNLS is brought into standard form by rescaling the remaining parameters once more, yielding an extra freedom due to discretization. Conversely, in order to take the continuum limit of Eq. (6) one has to let $\phi_n, \delta, \gamma, h \to 0$ and simultaneously keep the following ratios fixed:

$$\frac{\delta}{\gamma} = \frac{1}{\Gamma} = \text{const}, \quad \frac{2\gamma^3}{h^2} = \frac{\Gamma^3}{H^2} = \text{const}. \quad (7)$$

We are now going to analyze the stationary DNLS (6) for complex ϕ_n in terms of a 4D mapping

$$\mathbf{z}_{n+1} = \mathbf{F}(z_n) + \mathbf{G}(z_n), \quad \mathbf{z}_n = \begin{pmatrix} \mathbf{q}_n \\ \mathbf{p}_n \end{pmatrix}, \quad \mathbf{q}_n = \mathbf{p}_{n+1} = \begin{pmatrix} \text{Re}(\phi_n) \\ \text{Im}(\phi_n) \end{pmatrix} \quad (8)$$

with

$$\mathbf{F}(\mathbf{z}_n) = \begin{pmatrix} -\mathbf{p}_n + 2\mu \dfrac{\mathbf{q}_n}{\mathbf{q}_n^2 + 1} \\ \mathbf{q}_n \end{pmatrix},$$

$$\mathbf{G}(\mathbf{z}_n) = \begin{pmatrix} 2\dfrac{\gamma\mathbf{q}_n \times \mathbf{e}_\perp - h\mathbf{e}_{\text{Re}}}{\mathbf{q}_n^2 + 1} \\ \mathbf{0} \end{pmatrix}, \quad (9)$$

$\mathbf{e}_\perp$ being the unit vector normal to the complex ϕ_n plane and $\mathbf{e}_{Re}$ the unit vector in the real direction. One verifies easily that Eq. (8) is volume preserving even if $\gamma, h \neq 0$. Thus, the damping term $i\gamma\psi_n$ of the pde (1) plays the role of a conservative perturbation in the mapping.

Furthermore, in the unperturbed case ($\mathbf{G}=\mathbf{0}$) the mapping is symplectic and completely integrable [15]. The integrability follows from the two analytic invariants

$$I_1(\mathbf{z}_n) = (1+\mathbf{q}_n^2)(1+\mathbf{p}_n^2) - 2\mu\mathbf{q}_n \cdot \mathbf{p}_n, \qquad (10a)$$

$$I_2(\mathbf{z}_n) = (\mathbf{q}_n \times \mathbf{p}_n) \cdot \mathbf{e}_\perp. \qquad (10b)$$

and the symplectic structure from the invariant Poisson bracket $\{\mathbf{p}_n, \mathbf{q}_n\} = \mathbf{I}_2$, with $\mathbf{I}_2$ the 2×2 unit matrix. This symplectic structure can be shown to persist in the case $\gamma, h \neq 0$. In the case of zero damping we find that one integral is conserved in the modified form

$$I_1(\mathbf{z}_n) = (1+\mathbf{q}_n^2)(1+\mathbf{p}_n^2) - 2\mu\mathbf{q}_n \cdot \mathbf{p}_n - 2h(\mathbf{q}_n + \mathbf{p}_n)\mathbf{e}_{Re}. \quad (11)$$

It is worth noting that in the completely integrable case, ($\mathbf{G}=\mathbf{0}$), all solutions of this mapping can be parametrized in terms of Jacobi elliptic functions [20]. For the purpose of this paper, however, we shall be concerned only with homoclinic solutions. Since $\mu = 1 + \delta > 1$, the $\gamma = h = 0$ system (8) has a saddle point at the origin with a 2D unstable (and a 2D stable) manifold, on which the solutions are given by a two parameter family of homoclinic orbits. The union of these solutions (also called *homoclinic connection*) is an essential ingredient of the Mel'nikov analysis carried out in Sec. II B below. The homoclinic connection is given by $\hat{\mathbf{z}}_n = (\hat{\mathbf{q}}_n, \hat{\mathbf{p}}_n)$ with

$$\hat{\mathbf{q}}_n(\tau, \theta) = \hat{\mathbf{p}}_{n+1}(\tau, \theta) = \pm \begin{pmatrix} S_n(\tau)\cos\,\theta \\ S_n(\tau)\sin\,\theta \end{pmatrix}, \qquad (12)$$

where

$$S_n(\tau) = \sinh w \; \mathrm{sech}(nw + \tau), \quad w = \cosh^{-1}\mu, \quad 0 \leq \tau < w. \qquad (13)$$

For the derivation of Eq. (12), the parametrizing variables τ and θ play the role of time in a Hamiltonian flow with the integrals (10) being the corresponding Hamilton functions (see Appendix A). In fact, τ can be thought of as an interpolating variable between the flow and successive iterations of the map. The corresponding interpolation period w is almost equal to the lattice constant since $w = \cosh^{-1}(1+\Delta^2/2) \approx \Delta - \Delta^3/24$. It is also related to the largest eigenvalue λ^+ of the origin by

$$w = \cosh^{-1}\mu = \ln(\mu + \sqrt{\mu^2 - 1}) = \ln\lambda^+. \qquad (14)$$

A. Flat solutions and the upper boundary for breathers

By virtue of Eqs. (8) and (9) the real and imaginary parts of any stationary solution of the DNLS are given by the first two components of the phase vector $\mathbf{z}$. In particular, as explained in Sec. I, breather solutions can be identified with orbits that asymptotically go to a constant value, emerging from and ending at a fixed point. In $2N$-dimensional symplectic mappings the eigenvalues of fixed points can be

TABLE I. Existence of fixed points r_i, $i = 0,1,2,3$ in intervals of damping γ and driving h.

	$0 < \gamma < \delta/\sqrt{3}$	$\delta/\sqrt{3} < \gamma$
$h_+ < h$	$r_1 < r_-$	
$h_- < h < h_+$	$r_1 < r_- < r_2 < r_+ < r_3$	r_0
$h < h_-$	$r_+ < r_3$	

grouped in pairs with their product being unity for each pair [21]. Consequently, DNLS breathers can emerge only from such fixed points where all eigenvalues of the 4D map linearized about the fixed point are off the unit circle; i.e., there exist two stable and two unstable modes. (Indeed it is not sufficient to have only one pair of eigenvalues hyperbolic and the other elliptic, since this would lead to either asymptotically oscillating homoclinic or to heteroclinic solutions that have been excluded from the present treatment.)

We first identify all fixed points and consider their stability under iterations of the mapping. Every such fixed point of Eq. (8) represents a flat solution of the stationary DNLS (6), defined by

$$\phi_n = \phi_{n+1} = \sqrt{r}e^{i\theta} = \frac{r}{h}(\delta - r + i\gamma) \qquad (15)$$

for all n. The squared modulus r of this solution satisfies the cubic equation

$$P(r) = r[(r-\delta)^2 + \gamma^2] - h^2 = 0 \qquad (16)$$

and the phase θ is given by

$$\tan\,\theta = \frac{\gamma}{\delta - r}. \qquad (17)$$

Both equations are exact rescaled [with Eq. (5)] versions of the corresponding equations for the NLS; cf. [7]. Depending on the damping and driving parameters, Eq. (16) may have either one real solution r_0 (for $\gamma > \delta/\sqrt{3}$) or three real solutions (for $0 < \gamma < \delta/\sqrt{3}$). In the latter case the three amplitudes r_i, $i = 1,2,3$, are separated from one another by the extrema $r_\pm$ of the polynomial $P(r)$ in Eq. (16) such that $r_1 < r_- < r_2 < r_+ < r_3$ with

$$r_\pm = \frac{2\delta}{3} \pm \frac{1}{3}\sqrt{\delta^2 - 3\gamma^2}. \qquad (18)$$

Furthermore, these fixed points exist only in the driving regime $h_- < h < h_+$ with

$$h_\pm(\gamma) = \frac{\sqrt{6}}{9}\sqrt{\delta^3 \pm (\delta^2 - 3\gamma^2)^{3/2} + 9\delta\gamma^2}. \qquad (19)$$

At either boundary of this interval two of the fixed points annihilate in a saddle node bifurcation (r_1 and r_2 at h_+, r_2 and r_3 at h_-). All this is summarized in Table I.

The stability of each fixed point depends crucially on the sign of the polynomial in Eq. (16) evaluated at $r = \gamma$. It is easily seen that this sign changes when h varies across
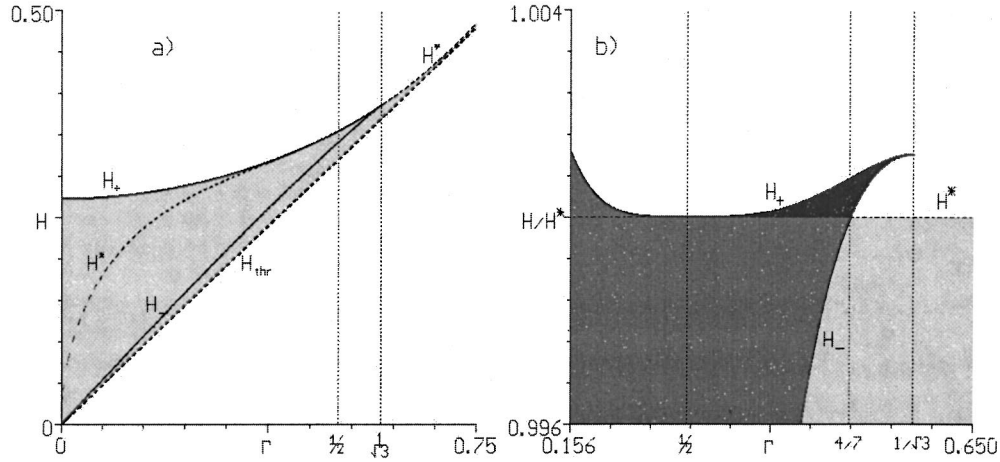
FIG. 1. Breather phase diagram in NLS parameters (driving H vs damping Γ) with lattice constant $\Delta = 0.2$. (a) Existence domain of breathers (shaded). (b) Fixed point existence and stability regions [vertical axis rescaled with $H^*(\Gamma)$]. Shades as follows: 1 elliptic point (white), 1 hyperbolic point (light gray), 1 elliptic, 1 hyperbolic, and 1 mixed point (gray), 2 elliptic points and 1 mixed point (black). The regions, which are shown here only near the the critical point $\Gamma = 1/2$, extend to the rest of the phase diagram shown in (a).

$$h^*(\gamma) = \sqrt{2\gamma^3 - 2\delta\gamma^2 + \delta^2\gamma}. \qquad (20)$$

The stability analysis for each fixed point in its respective existence regime is carried out in Appendix B. We distinguish several regions of the plane h versus γ, which must be studied individually while the resulting phase diagram contains five regions of qualitatively different behavior.

These regions are best observed in the neighborhood of the point $\gamma = \delta/2, h = h^*(\gamma) = h_+(\gamma)$, as shown in Fig. 1(b). For weak driving (light shade) we find one double-hyperbolic fixed point. It coincides with r_0 for strong damping $\gamma > \delta/\sqrt{3}$ and with r_1 otherwise. For strong driving (white) there exists one stable fixed point, given for strong damping by r_0 and otherwise by $r_3(h > h_+), r_1(h < h_-)$. Both fixed points persist in the darker region where they are accompanied by a mixed (hyperbolic-elliptic) fixed point r_2. The fourth region (black) is limited horizontally to the tiny interval of moderate damping $\delta/2 < \gamma < \delta/\sqrt{3}$ and vertically in between h_+ and h^*. It does not contain a double hyperbolic fixed point and here the points r_1 and r_3 are both stable whereas r_2 remains of mixed type. Finally, for ultrastrong driving $h > 2$, there exists another region where the stable fixed point $r_3(r_0)$ changes into an unstable elliptic-hyperbolic one not visible in Fig. 1 (cf. Appendix B).

From the condition formulated in Sec. I we conclude that breathers can only exist in regions 1 and 3. Hence the upper boundary of the existence domain is

$$h_+(\gamma), \quad \gamma \lessgtr \delta/2 \quad \text{and} \quad h^*(\gamma), \quad \gamma \gtrless \delta/2. \qquad (21)$$

The global phase diagram is presented in Fig. 1(a) in which the shaded region denotes the domain of existence of breather solutions. In the regime of moderate damping $\delta/2 < \gamma < \delta/\sqrt{3}$ the functions h^* and h_+ are graphically indistinguishable since their difference is less than $(\frac{1}{10}\sqrt{\delta})^3$, with $h_+ \geq h^*$. At the critical point $\gamma = \delta/2$ the two functions match and so do their first, second, and third derivatives with respect to γ.

So far, our analysis of the upper branch of the existence domain coincides with that of Barashenkov and Smirnov for

the NLS, after rescaling with the lattice spacing. The lower existence boundary, on the other hand, differs somewhat from the continuous case, as explained in the next subsection.

B. Homoclinic tangency and lower boundary for breathers

As mentioned above, the stationary DNLS with damping and driving can be described using a 4D mapping (8), (9). Since the solutions of the integrable part $\mathbf{F}$ are known explicitly, one can apply a Mel'nikov approach to derive conditions that are necessary for the existence of homoclinic orbits. Thus, in order to treat the term $\mathbf{G}$ as a perturbation we take h and γ small. Considering the scaling relation (5) this may also include the case of large H and Γ provided that the lattice constant Δ is small enough.

More generally, one can develop a Mel'nikov analysis of $2N$-dimensional mappings of the type (8) if the integrable term $\mathbf{F}$ has the following two properties: It possesses a hyperbolic fixed point with a homoclinic (heteroclinic) connection and this fixed point transforms smoothly as $\mathbf{G}$ increases while its stability properties remain unaffected. We then say that the fixed point survives the perturbation. No restrictions need be imposed on $\mathbf{G}$ apart from boundedness.

One then can construct a vector function $\mathbf{M}$, called the Mel'nikov vector [15], which is related to the distance between the invariant manifolds of the hyperbolic point of the nonintegrable composite mapping $\mathbf{F} + \mathbf{G}$. More precisely, the projections of these manifolds onto the homoclinic connection of the integrable mapping $\mathbf{F}$ yield components of $\mathbf{M}$, to lowest order in a small parameter proportional to $\mathbf{G}$. Transversal zeros of $\mathbf{M}$ correspond to homoclinic points which, in our DNLS application, yield solitonlike solutions [16]. Tangential zeros, on the other hand, are obtained at critical parameter values where homoclinic orbits are created (or cease to exist) in a global bifurcation. The general form of the Mel'nikov vector is given by [15]

$$M_k(\mathbf{t}) = \sum_{n=-\infty}^{\infty} \widetilde{\mathbf{q}}_{n+1}^{(k)}(\mathbf{t}) \cdot \mathbf{G}(\hat{\mathbf{z}}_n(\mathbf{t})), \quad k = 1, \dots, K, \qquad (22)$$

$\hat{\mathbf{z}}_n \in \mathbf{R}^{2N}$ being the separatrix solutions on the homoclinic connection of $\mathbf{F}$ parametrized by $\mathbf{t} \in R^N$. K is the dimension of the bounded subspace of the variational solutions of $\mathbf{F}$, and $\tilde{\mathbf{q}}_n^{(k)}$ is the kth independent solution of the adjoint variational problem. These solutions are readily obtained from the constants of motion I_k via

$$\tilde{\mathbf{q}}_n^{(k)}(\mathbf{t}) = \nabla_{\mathbf{z}} I_k(\hat{z}_n(\mathbf{t})). \tag{23}$$

Since $\mathbf{M}$ is obtained from the first order variational equations of the perturbed mapping, the error in measuring distances between the invariant manifolds is quadratic in the size of the perturbation $\mathbf{G}$. Numerical calculations of homoclinic tangency carried out in [15] suggest that the size of the perturbation can be defined using a suitable (maximum) norm.

Now, as shown in the previous subsection, the double hyperbolic fixed point, for $\mathbf{G}=\mathbf{0}$ located at the origin, survives the perturbation for γ and h in the range (21). Thus, in this range we can apply the Mel'nikov theory developed in [15] to the 4D map of the periodically driven damped DNLS as follows.

First we use Eq. (23) to derive the adjoint variational solutions from the integrals (10) yielding

$$\tilde{\mathbf{q}}_n^{(1)} = 2\begin{pmatrix} \hat{\mathbf{q}}_n(1+\hat{\mathbf{p}}_n^2) - \mu\hat{\mathbf{p}}_n \\ \hat{\mathbf{p}}_n(1+\hat{\mathbf{q}}_n^2) - \mu\hat{\mathbf{q}}_n \end{pmatrix}, \quad \tilde{\mathbf{q}}_n^{(2)} = \begin{pmatrix} \hat{\mathbf{p}}_n \times \mathbf{e}_\perp \\ \mathbf{e}_\perp \times \hat{\mathbf{q}}_n \end{pmatrix}. \tag{24}$$

whence the Mel'nikov vector (22) can be calculated using Eqs. (9), (12), (13), and (24). In particular, one finds that the first component of $\mathbf{M} = (M_1, M_2)$ vanishes identically:

$$M_1 = 4\sum_n [\hat{\mathbf{q}}_{n+1}(1+\hat{\mathbf{q}}_n^2) + \mu\hat{\mathbf{q}}_n] \frac{\gamma\hat{\mathbf{q}}_n \times \mathbf{e}_\perp - h\mathbf{e}_{\text{Re}}}{\hat{\mathbf{q}}_n^2 + 1}$$

$$= 4\gamma I_2 - 2h\sum_n (\hat{\mathbf{q}}_{n-1} - \hat{\mathbf{q}}_{n+1})\mathbf{e}_{\text{Re}} = 0, \tag{25}$$

where we have used the mapping (8) for $\gamma = h = 0$, setting $I_2 = 0$ on the homoclinic connection (since θ is independent of n).

The second Mel'nikov component is given by

$$M_2 = 2\sum_n (\hat{\mathbf{q}}_n \times \mathbf{e}_\perp) \frac{\gamma\hat{\mathbf{q}}_n \times \mathbf{e}_\perp - h\mathbf{e}_{\text{Re}}}{\hat{\mathbf{q}}_n^2 + 1}$$

$$= 2\gamma\sum_n \frac{S_n^2}{S_n^2 + 1} - 2h\sin\theta\sum_n \frac{S_n}{S_n^2 + 1}$$

$$= \frac{2}{\mu}\left\{ \gamma\sum_n S_n S_{n+1} - h\sin\theta\sum_n S_n \right\} \tag{26}$$

in which we have made use of Eq. (13) and the following identity of the hyperbolic functions:

$$2\cosh w \ \text{sech} \ x = (1 + \sinh^2 w \ \text{sech}^2 x)$$

$$\times [\text{sech}(x-w) + \text{sech}(x+w)],$$

$$x, w \in \mathbf{R}. \tag{27}$$

It is interesting to note that the vanishing of M_1 for all γ and h may be related to the fact that (a) M_1 is independent of γ and (b) the system possesses an integral for $\gamma = 0$, i.e., Eq. (11). This integral could, in principle, by used to reduce the 4D system (9) to a nonintegrable 2D map in the case $\gamma = 0$, $h \neq 0$. Furthermore, the identical vanishing of M_1 implies that under suitable conditions one may anticipate a one parameter family of zeros of the Mel'nikov vector, in contrast to the case of two or more coupled DNLS systems ([16]) where the zeros occur only at isolated points.

Let us now concentrate on the case of homoclinic tangency. Following [15,16] the invariant manifolds intersect tangentially if and only if at some points $\mathbf{t}^* = (\tau^*, \theta^*)$ on the homoclinic connection

$$\mathbf{M}(\mathbf{t}^*) = 0, \quad \det[\partial\mathbf{M}(\mathbf{t}^*)/\partial\mathbf{t}] = 0, \tag{28}$$

and an extra nondegeneracy condition holds on the second derivatives of $\mathbf{M}$. In our case, however, due to the fact that the determinant of the Jacobian in Eq. (28) vanishes, this nondegeneracy condition is violated everywhere on the homoclinic connection.

One way to overcome this problem is to relax the tangency condition by requiring only that the partial derivatives of M_2 vanish at some points $\mathbf{t}^*$. This modified notion of tangency is sufficient to obtain the threshold function $h_{\text{thr}}(\gamma)$, as shown below.

Note that for our mapping the tangency equations

$$\mathbf{M}(\mathbf{t}^*) = 0, \quad \partial M_2(\mathbf{t}^*)/\partial\mathbf{t} = 0 \tag{29}$$

are satisfies with $\theta^* = \pm\pi/2$ and can be rewritten in terms of τ^* using Eq. (26) as

$$\pm\frac{h}{\gamma} = q(\tau^*) = \frac{\partial}{\partial\tau} q(\tau^*), \tag{30}$$

where the choice of signs corresponds to the sign of θ^* and $q(\tau)$ is defined by

$$q(\tau) = \frac{\sum S_n(\tau)S_{n+1}(\tau)}{\sum S_n(\tau)}. \tag{31}$$

For small lattice spacing Δ, implying $w \to 0$, the evaluation of Eq. (30) is straightforward: Replacing the sums in Eq. (31) by integrals one finds

$$\sum_{n=0}^{\infty} S_n(\tau) \approx \sinh w \int_{-\infty}^{\infty} \text{sech} \ t dt = \pi \sinh w, \tag{32a}$$

$$\sum_{n=-\infty}^{\infty} S_n(\tau)S_{n+1}(\tau) \approx \sinh^2 w \int_{-\infty}^{\infty} \text{sech} \ t \ \text{sech}(t+w)dt$$

$$= 2w \sinh w. \tag{32b}$$

With these estimates the tangency threshold below which no homoclinic points exist follows from the first equality in Eq. (30) as
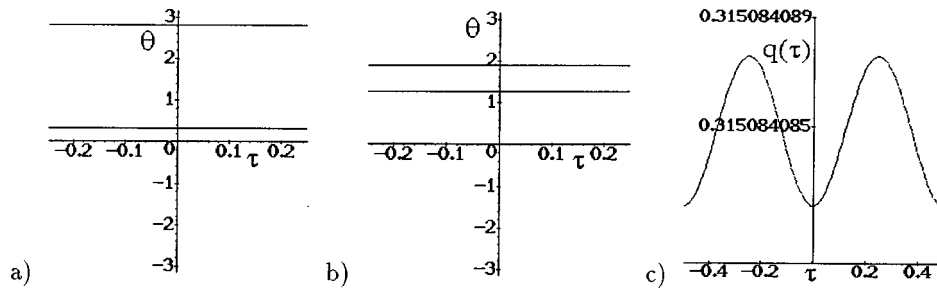
$$h_{\text{thr}}(\gamma) = \frac{2w}{\pi}\gamma. \tag{33}$$

FIG. 2. Nodelines of the Mel'nikov component M_2 over a unit cell $\tau \in [-w/2, w/2]$, $\theta \in [-\pi, \pi]$. (a) $h = \Delta\gamma$, (b) $h = \Delta\gamma/3$. (c) Mel'nikov ratio $q(\tau)$, $\tau \in [-w, w]$. Note that $q(\tau)$ depends very weakly on τ even for large discretization Δ, here $\Delta = 1/2$, $w = \cosh^{-1}(1 + \Delta^2/2) \approx \Delta$.

Next we consider the effects of discretization. For lattice spacings considerably larger than zero the infinite sums in Eq. (31) cannot be calculated analytically. Also the subsequent application of the Poisson formula and residue theory, by which other types of perturbed NLS equations are tractable [20,14], fails here due to removable singularities. Thus we restrict our discussion to specific values of τ.

From the fact that both sums in Eqs. (31) are w periodic and symmetric at the points $\tau = 0$ and $\tau = w/2$, it follows that they also have extrema at these points. More precisely, 0 is a minimum and $w/2$ a maximum of $q(\tau)$. It is therefore reasonable to assume that, as the driving increases and the second Mel'nikov component (26) decreases, M_2 will vanish first at the point $\tau^* = 0$. Some numerical results concerning the zeros of the Mel'nikov vector that are obtained from the relation $\gamma q(\tau) = h \sin\theta$ and the ratio $q(\tau)$ in the case $\Delta = 1/2$ are presented in Fig. 2. Note that even for this rather large value of Δ the variation in $q(\tau)$ is very small. Using the exponential decay of the sech function we evaluate the infinite sums at $\tau = 0$ replacing them by their partial sums with $|n| \leqslant Nw$. Typically with $N = 5$ the remainder can be neglected. For sufficiently small values of w, $q(0)$ can be expanded in powers of w yielding the threshold value

$$h_{\text{thr}} = \gamma q(0) = \frac{2}{\pi} \gamma \left[w + \frac{1}{6} w^3 + O(w^4) \right]. \qquad (34)$$

In this way we recover the previous result for small spacings, plus corrections of third order in w. The inequality $h > h_{\text{thr}}$ can be considered as a necessary condition for the existence of breather solutions. Numerical calculations of breathers all point to the fact that indeed for all h values larger than h_{thr} and smaller than h_+ (h^* for large damping) such solutions can be found.

Now we are in a position to describe the effects of discretization on the lower existence boundary. Equation (34) expressed in the NLS parameters, cf. Eq. (5), gives

$$H_{\text{thr}} = \frac{2}{\pi} \Gamma [1 + \tfrac{1}{8} \Delta^2 + O(\Delta^3)]. \qquad (35)$$

This result confirms and generalizes to second order the boundary given for the NLS by three independent perturbative methods [6,22,19]. The numerical computations of the lower existence boundary of the NLS by Barashenkov and

Smirnov [7] show small deviations from Kaup and Newell's linear law [6], but not more than 10^{-3} even for large values H and Γ.

One can even show that our DNLS result gives the exact threshold of the continuous NLS system: Taking in Eq. (35) the continuum limit $\Delta \to 0$ and arguing that the Mel'nikov analysis in this case is accurate for all $\gamma, h \to 0$, the exact validity of the linear law is verified even for large values H and Γ.

Of course the question arises whether the corrections in Eq. (35) are of any significance, since they have been obtained by a perturbative Mel'nikov treatment. Noting, however, that the Mel'nikov error is of second order in the perturbation, one sees immediately that Mel'nikov inaccuracies caused by finite values of $\gamma \sim \Delta^2$ enter only at fourth order in Δ while those caused by $h \sim \Delta^3$ occur at sixth order. Consequently, the second (even third) order in Δ correction to the threshold (35) is purely due to the discretization.

III. SINGLE-HUMP STRUCTURES (BREATHERS)

A. Stationary solutions

In the domain of existence of the DNLS solitons, defined by Eqs. (21) and (34), we find a pair of stationary single-hump solutions emerging from the flat background. On the line $\gamma = 0$ they are real and have the exact form

$$\phi_n^{\pm} = \psi_n^{\pm}(t=0)$$
$$= \sqrt{r} \left(1 + \frac{2a}{1 \pm \sqrt{b} \cosh(n \cosh^{-1} \kappa + r\tau)} \right), \qquad (36)$$

where r is the smallest root of Eq. (16), $\tau \in \mathbf{R}$ is a free parameter and

$$\kappa = \frac{1 + \delta - 2r}{1 + r}, \qquad a = \frac{(3 + \delta)(1 - \kappa)}{2(\kappa - 1 - \delta)},$$

$$b = 1 + \frac{a}{1 + \delta(1 + a)/(2a + 3)}. \qquad (37)$$

In agreement with [12,13] we shall call such single-hump structures breathers, owing to the fact that they are oscillatory functions of time. Both are very similar to the corresponding breather solutions of the NLS [7], the three constants in Eq. (37) differ from their continuum values in such
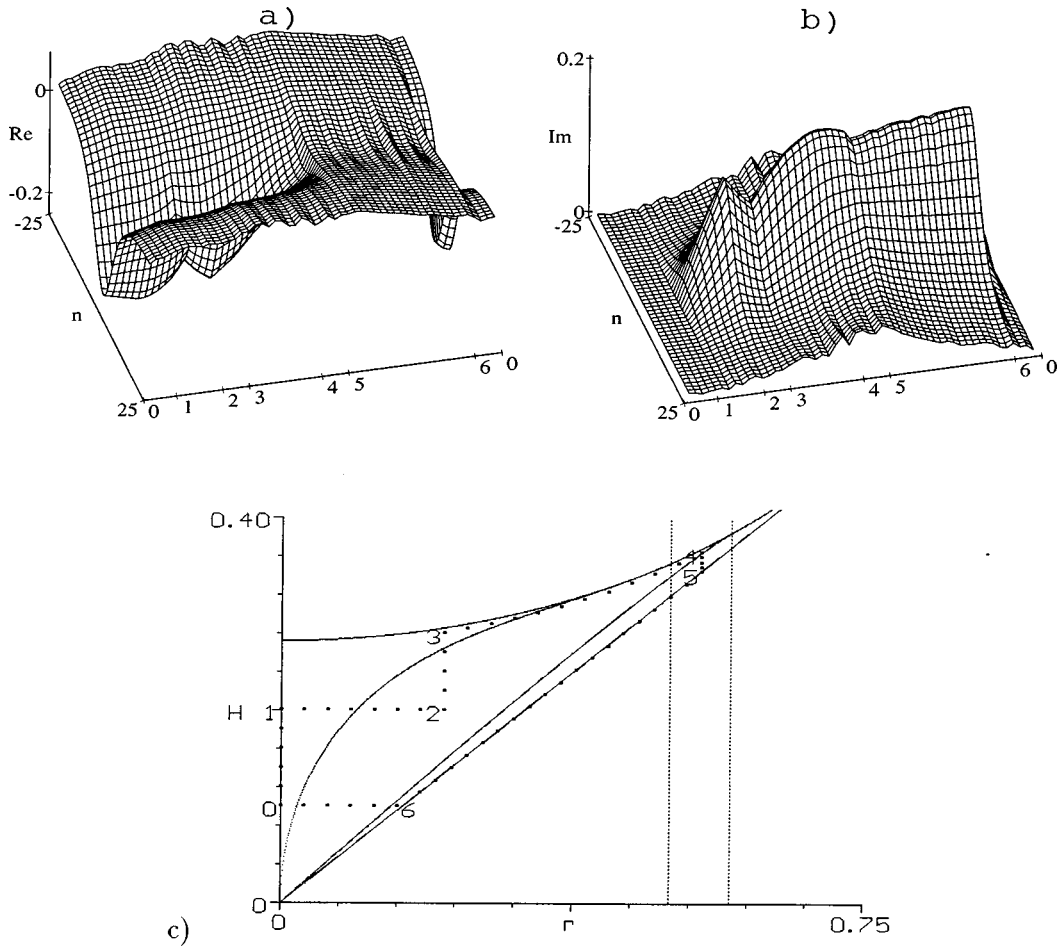
FIG. 3. Variation of ϕ^- along a path in the (Γ, H) plane. (a) Re(ϕ^-), (b) Im(ϕ^-), (c) the path (dotted). In (c) the curves H_{thr}, H_-, H^*, H_+ and vertical lines $\Gamma = 1/2, \Gamma = 1/\sqrt{3}$ are drawn for clarity. $\Delta = 0.2$.

a way that in the continuous limit κ approaches unity and $a, b \to \infty$, $a/b \to 1$, in agreement with $\psi_n = \Delta \Psi(n\Delta)$. Similarly, in the integrable limit $h = 0$ the sech solution is recovered, with the difference that here $\kappa = \mu$ and $a, b \to \infty$, $a/b \neq 1$. The calculations leading to these constants are given in Appendix C.

The fact that the breather solutions (36) appear as one-parameter families in τ is directly related to the existence of an integral I_1, i.e., Eq. (11). As already mentioned earlier, this integral may be used to reduce the stationary DNLS to a family of 2D mappings all displaying homoclinic chaos in two dimensions. The pair of homoclinic orbits of each of these mappings is given by Eq. (36) for particular values of the parameter τ.

The behavior of these breathers as functions of the parameters of the problem can be seen if we follow them ''adiabatically'' along a path in the parameter plane. This is accomplished by starting with the analytical solution (36) with $\tau = 0$, somewhere on the line $\gamma = 0$ and adjusting it numerically as h and γ are varied. In Fig. 3 this procedure is shown for ψ^-. Increasing the driving h, i.e., moving from 0 to 1 in Fig. 3, ψ^- becomes more pronounced as the minimum of its real part becomes deeper. Proceeding then away from the line $\gamma = 0$ (from 1 to 2) an imaginary part appears. Moving towards the upper boundary (from 2 to 3), the ψ^+ breather (not shown) flattens out, becoming eventually equal to the constant background at h^+. At the same time, ψ^- remains

well localized and stays that way along the boundary (from 3 to 4). ψ^+ cannot be followed here, since it is indistinguishable from the fixed point. Decreasing the driving away from the upper bound, ψ^+ emerges again, and in approaching the threshold the two solutions ψ^- and ψ^+ tend to coincide (line 4 to 5). On the threshold line the real part of the solutions vanishes exactly at the center ($n = 0$) and remains small at all other lattice sites. Here the phase angle between the real and imaginary parts, taken at the breather's center, approaches the value $\pi/2$ from above for ψ^+ and from below for ψ^-, in agreement with the Mel'nikov variable θ^* at homoclinic tangency; compare Fig. 2(c). The behavior sketched above in approaching the threshold with both solutions being nearly equal persists if we decrease the driving along a path slightly above the threshold (5 to 6). When we finally switch off the damping at constant h the difference between both solutions increases again until we reach the point 0 we started from.

B. Time evolution

The problem of stability of the solutions (36) in time has been discussed in detail for the continuous system [7] by discretizing the damped driven NLS in a non-Ablowitz-Ladik manner and formulating an eigenvalue problem for the discretized version. The numerical solution of this linear problem reveals that the bright soliton Ψ^+ is always un-
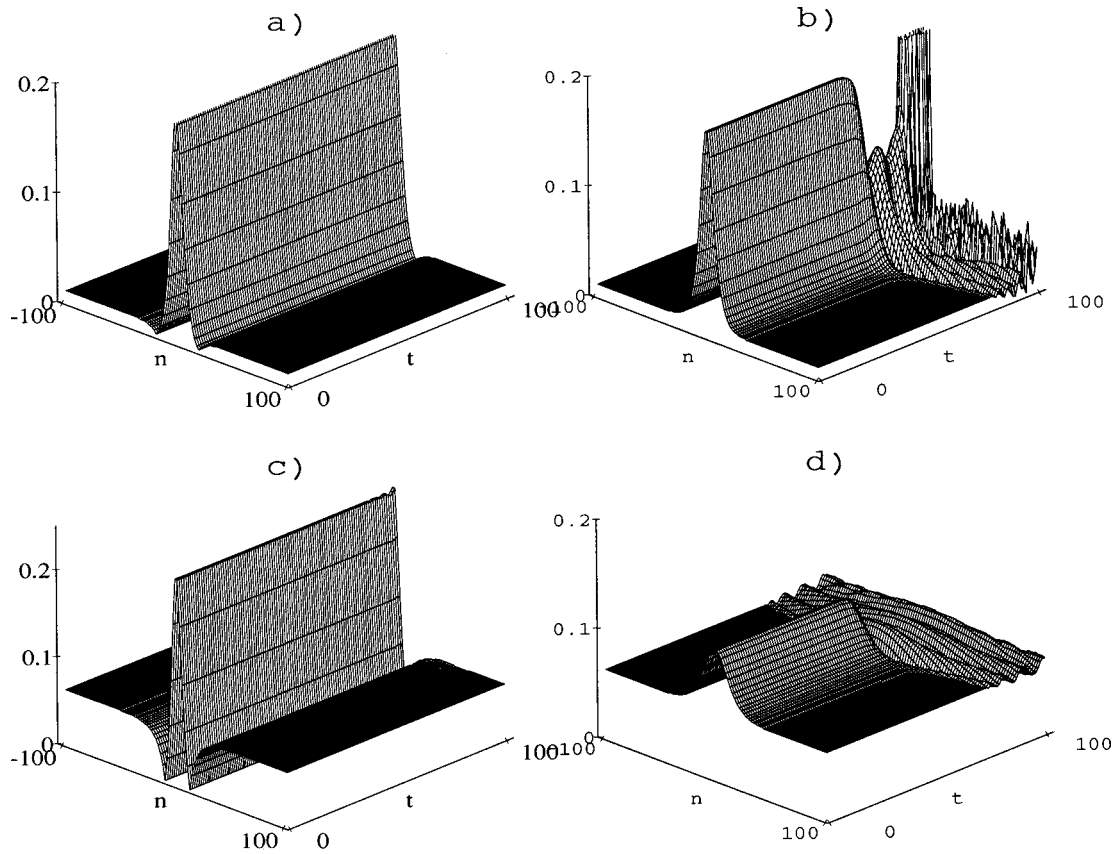
FIG. 4. Modulus $|\psi_n^\pm(t)|$ of breathers (36) in time, for $\Gamma=0$. Upper row: $H=0.05$, (a) ψ^-, (b) ψ^+. Lower row: $H=0.25$, (c) ψ^-, (d) ψ^+. $\Delta=0.2$. Note the stability occurring at $t\approx100$ in (c).

stable, whereas the dark soliton Ψ^- is stable below a line $H_{\mathrm{st}}(\Gamma)$ with $H_{\mathrm{st}}\approx0.08$ as $\Gamma\to0$. This fact is interpreted as follows: Below the line $H_{\mathrm{st}}(\Gamma)$ the spectrum of the dark solution is bounded from the right by the value of Γ implying stability, whereas above H_{st} a single pair of eigenvalues acquires a real part larger than Γ, which makes the dark solution unstable.

For the DNLS system investigated here the stability properties are qualitatively the same as in the NLS case in the sense that a similar stability threshold h_{Hopf} of the dark solution ψ^- appears to exist. In Fig. 4 we show numerical integrations for both solutions (36), which indicate that the times needed for break down due to numerical errors are enormous. At a value of h corresponding to $H=0.05$ the ψ^+ breather begins to deviate from its initial shape at $t\approx60$ while ψ^- remains stable for at least $t=500$. Even at $H=0.25$, which is close the upper existence boundary, the solutions are numerically stable up to $t\approx100$, corresponding to 20 000 iterations of the numerical time integration scheme.

On the line $\gamma=0$ it can be shown exactly that both solutions are marginally stable. This is explained as follows: Rewriting $\psi_n^\pm(t)=u_n(t)\exp(it)$, the DNLS (1) becomes

$$i\delta u_n + \frac{u_{n+1}+u_{n-1}}{2}(1+|u_n^2|)=(\mu-i\gamma)u_n-h \quad (38)$$

whence the stability of the breathers is determined by the spectrum of the linearized flow $\dot\xi=\mathbf{J}\xi$ obtained from inserting $u_n=\phi_n^\pm+\xi_n$ in Eq. (38), where $\mathbf{J}$ is the Jacobian matrix with matrix elements

$$J_{nm}=\frac{\partial u_n}{\partial u_m}(\phi_n^\pm)=\frac{1}{i\delta}\left\{\frac{\mu-i\gamma+h\phi_n^{\pm*}}{1+|\phi_n^\pm|^2}\delta_{n,m}\right.$$
$$\left.-\frac{1+|\phi_n^\pm|^2}{2}(\delta_{n+1,m}+\delta_{n-1,m})\right\}, \quad (39)$$

where $\delta_{n,m}$ is the Kronecker delta, the asterisk denotes complex conjugation, and we have used the mapping (6).

For $\gamma=0$, the $\phi_n^\pm$ are real and the matrix $i\delta\mathbf{J}$ is a real almost symmetric matrix with real eigenvalues. Thus, the spectrum of Eq. (38) is located on the imaginary axis, meaning that both the dark and the bright solutions are marginally stable in time. It would be interesting to check from Eq. (38) that for $\gamma\neq0$ there is indeed a stability threshold h_{st} in agreement with the numerical results (see Fig. 5 for a specific value of $\Gamma=0.2$).

It is interesting to remark that the ψ_n^+ breather can be made stable by modifying the boundary conditions of the DNLS (1). Namely, enforcing at finite lattice sites $n=\pm N$ (typically $N=50$) the value of the flat solution $\psi_n(t)=\sqrt{r}e^{it}$, the modulus of the bright soliton exhibits oscillations in time with a frequency that increases with h, yet displaying always a single hump in the spatial direction; cf. Fig. 6. Similar solutions, so-called whiskers, were discovered for the near integrable damped driven NLS under periodic boundary conditions and discussed in terms of Bäcklund transformations [23]. They also occur in arrays of linearly coupled optical fibers [24].
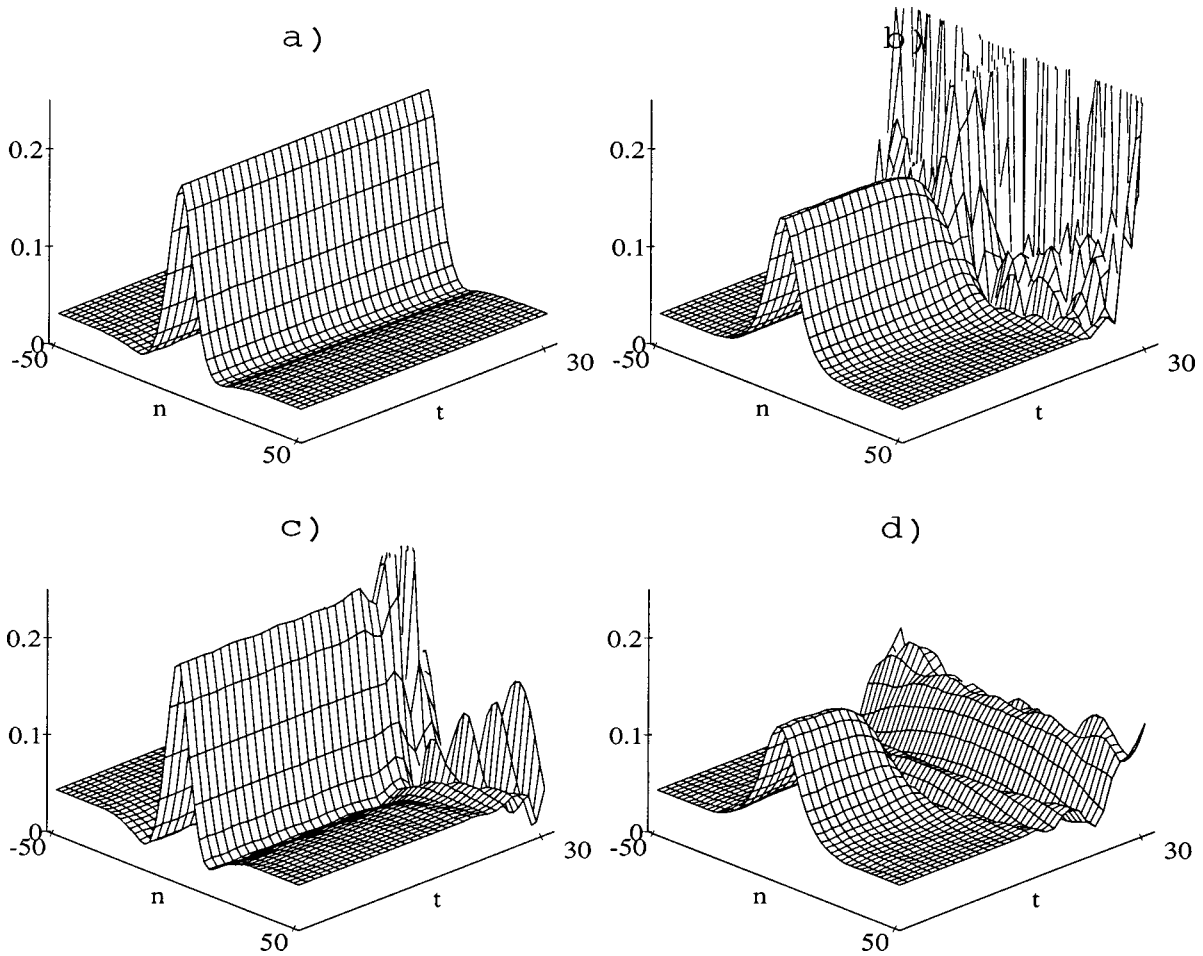
FIG. 5. Modulus $|\psi_n^{\pm}(t)|$ of breathers, for $\Gamma = 0.2$. Upper row: $H = 0.15$, (a) ψ^-, (b) ψ^+. Lower row: $H = 0.20$, (c) ψ^-, (d) ψ^+. $\Delta = 0.2$.

In our case, the numerical calculations show that the whisker solutions disappear at sufficiently large values of N (e.g., $N = 65$ in the case under consideration). This might be understood perhaps in terms of Poincaré recurrence times, which become very large for sufficiently large N, or by qualitative changes in the structure of high order resonances near the origin as the number of degrees of freedom increases.

IV. MULTIHUMP STRUCTURES (MULTIBREATHERS)

It was already observed in [7,18] that the NLS allows for other solutions beyond the single-hump structures discussed in the previous section. A number of multihump structures, in particular, with two and three humps, could be found by means of a variational method using combinations of single-hump solutions under an effective potential. In keeping with the terminology adopted in Sec. III, we shall call them multibreathers.

Numerical calculations performed on the damped driven DNLS show that this system of equations possesses a great variety of multibreathers, exhibiting different numbers of humps and obeying symmetry relations between individual solutions. In view of the large number of these solutions at almost any point in the existence domain, one would like to
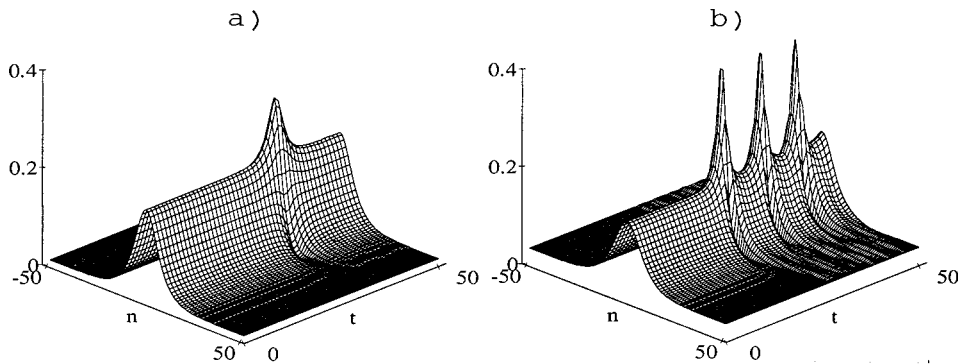

FIG. 6. Modulus $|\psi_n^{\pm}(t)|$ of whisker solutions found at $\Gamma = 0$. Initial wave $\psi_n(t=0) = \phi_n^+$. (a) $H = 0.05$, (b) $H = 0.15$. Flat background enforced at $n = \pm 50$. $\Delta = 0.2$.
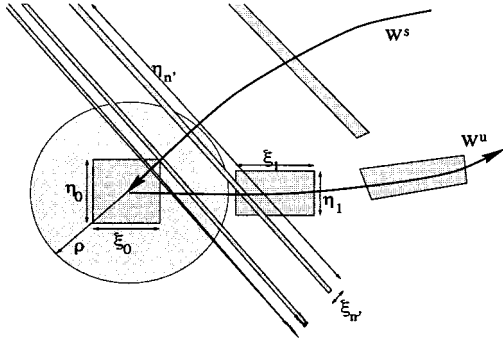
FIG. 7. Planar sketch of the 4D shooting algorithm. Lines represent 2D areas in phase space, areas represent 4D volumes.

classify them according to their increasing complexity.

It is beyond the scope of the present paper to give a complete classification. We therefore restrict ourselves to describe the numerical method employed for the construction of solutions and the symmetry classes of solutions. We also survey their occurrence in the (H, Γ) plane in terms of an area order parameter, illustrating our findings with a few representative examples. We hope to come to a more satisfactory picture at a later stage.

A. Shooting algorithm

The shooting algorithm we have employed to construct multibreather solutions of high complexity is capable of locating any solution with a finite number of humps. Furthermore, the method is not restricted to the model studied here, as it can be applied to other DNLS systems as well, such as the ones studied in [16]. Similar algorithms have been used in studies of pattern formation in complex Ginzburg-Landau systems with a continuous space variable [25]. Our method uses the smoothness of the unstable manifold W^u along the outgoing direction of the fixed point r. Furthermore, using symmetry relations we can avoid the complicated dynamics along the incoming direction.

The first step of the algorithm is accomplished by considering a small 4D cube centered around the hyperbolic fixed point z_∞. This cube will of course be distorted under successive iterations, as shown in Fig. 7, whence we define its dimensions dynamically by an area ξ_n along the unstable manifold W^u and a perpendicular area η_n, the sides of the initial cube being typically $\sqrt{\xi_0} = \sqrt{\eta_0} = 10^{-5}$. A phase point z_0 is now chosen randomly in this cube and iterated under the mapping. Upon return of this point to the neighborhood of z_∞ we check whether it enters a reference sphere of radius $\rho = 10^{-4}$ around z_∞. By doing so we isolate those initial conditions that are close to homoclinic points of the system.

This filter can be made exponentially sharp since the areas $\xi_n (\eta_n)$ of the 4D strip resulting from iterations of the initial cube shrink (spread) at an exponential rate upon return along the stable manifold W^s. The return probability π can be calculated from the overlap σ_n between the reference sphere and the nth iterate of the cube. With $n'(\rho)$ denoting the time upon reentrance in the ρ sphere the return probability is

$$\pi = \frac{1}{\sigma_0} \sum_{n=n'}^{\infty} \sigma_n = \frac{1}{\min(\rho^2, \xi_0) \min(\rho^2, \eta_0)}$$

$$\times \sum_{n=n'}^{\infty} \min(\rho^2, \xi_n) \min(\rho^2, \eta_n). \tag{40}$$

Having chosen $\xi_0 = \eta_0 \ll \rho^2$, this gives

$$\pi = c_g \frac{\rho^2}{\xi_0 \eta_0} \sum_{n=n'}^{\infty} \xi_n = c_g \frac{\rho^2}{\xi_0 \eta_0} \xi_{n'} \sum_{m=0}^{\infty} (e^{-\Lambda})^m$$

$$\approx c_g \frac{\rho^2}{\eta_0} \frac{\exp[-\Lambda(n'-n'')]}{1 - \exp(-\Lambda)}, \tag{41}$$

where $\Lambda > 0$ is the sum of the real parts of two stable eigenvalues of the fixed point z_∞, n'' is the first iterate for which homoclinic points within the strip are mapped close to the linearized stable manifold ($n'' \ll n'$), and c_g is a factor necessary to match the Cartesian geometry of the iterated strip to the reference sphere.

In a subsequent step, a solution is constructed by iterating a z_0 that was found to be close to a homoclinic point in step 1. This iteration procedure works well up to some iterate $n > n'$ at which the orbit approaches closely a point on the hyperbolic set within the reference sphere and subsequently escapes to regions far away from the hyperbolic fixed point. The solution is then extrapolated in a smooth way to the fixed point value. For a class of solutions, which are degenerate with respect to a reversing symmetry of the mapping (cf. Sec. IV C, below), the accuracy of this procedure can be enhanced by some orders of magnitude.

B. Symmetries

If solutions are symmetric with respect to n we can avoid iterating through the chaotic regime. We then determine the center of the orbit ($n=0$) and subsequently reflect the left wing of the solutions onto the right wing. To do so, one must first verify that the result delivered by the shooting algorithm is indeed symmetric with respect to n. This is achieved by the following symmetry argument.

Note that the mapping

$$\mathbf{S} \begin{pmatrix} \mathbf{q}_n \\ \mathbf{p}_n \end{pmatrix} = \begin{pmatrix} \mathbf{p}_n \\ \mathbf{q}_n \end{pmatrix}. \tag{42}$$

is a reversing symmetry of the stationary DNLS (8) since for all γ and h

$$\mathbf{S}(\mathbf{F} + \mathbf{G}) = (\mathbf{F} + \mathbf{G})^{-1} \mathbf{S}. \tag{43}$$

Consequently, our system allows for two kinds of orbits: symmetric ones with $z_n = \mathbf{S} z_n$ and nonsymmetric ones that occur in pairs, z_n and $\mathbf{S} z_n$.

An orbit is symmetric with respect to $\mathbf{S}$ if and only if it has a point in the fixed set of $\mathbf{S}$

$$\Phi^{\text{Fix}}(\mathbf{S}) = \{ \mathbf{z} | \mathbf{S}(\mathbf{z}) = \mathbf{z} \} = \{ \mathbf{z} | \mathbf{q} = \mathbf{p} \}; \tag{44}$$
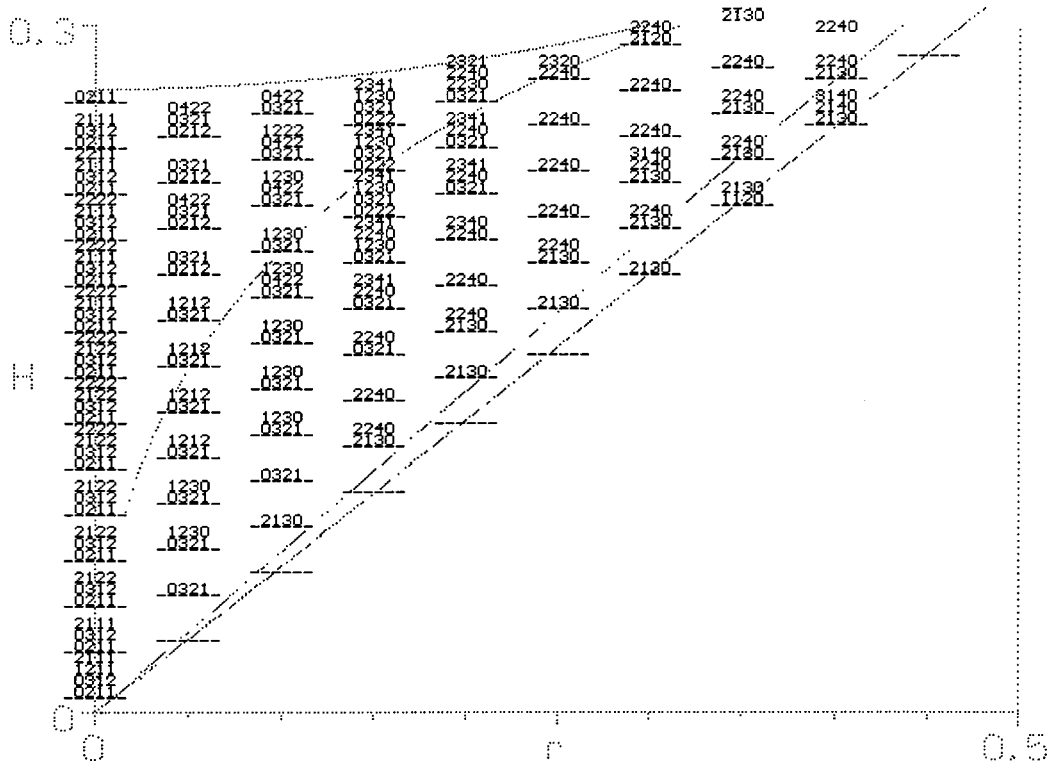
FIG. 8. Existence diagram of multibreathers localized within $|n| = \pm 75$. Driving values are indicated by dashed lines, all solutions found at a particular H value are indicated by a 4-digit code above the dashed line. The code $n_1 n_2 n_3 n_4$ symbolizes a solution with n_1 maxima and n_2 minima of the real part, n_3 maxima and n_4 minima of the imaginary part. Maxima are counted only above the flat background, minima only below. Note that solutions may change labels along a path in the parameter plane due to local bifurcations. Antisymmetric solutions (only at $\Gamma = 0$) with identical labeling are listed once. The curves H_{thr}, H_-, H^*, H_+ are drawn for orientation. $\Delta = 0.2$.

cf. [26]. In particular, since all fixed points of the mapping, including $\mathbf{z}_\infty$, lie in Eq. (44), the intersection of $\Phi^{\mathrm{Fix}}(\mathbf{S})$ with W^u (or W^s) contains at most points that are part of a symmetric orbit. We also need to consider the possibility that the intersection is empty, since $\Phi^{\mathrm{Fix}}(\mathbf{S})$ does not divide the phase space. This is exactly the case for drivings below the threshold. Yet, once the intersection of $\Phi^{\mathrm{Fix}}(\mathbf{S})$ with W^u (or W^s) has occurred, beyond the line h_{thr} of homoclinic tangency, this intersection is structurally stable. This follows from the fact that both $\Phi^{\mathrm{Fix}}(\mathbf{S})$ and W^u are two-dimensional manifolds whose intersection in 4D vector space is of codimension 2.

Focusing on our application to multibreathers, symmetric multihump solutions are distinguished from nonsymmetric ones by the fact that symmetric homoclinic orbits possess a point in $\Phi^{\mathrm{Fix}}(\mathbf{S})$ while nonsymmetric homoclinic orbits do not. In fact, although we cannot exclude the existence of nonsymmetric orbits, numerically we found only symmetric ones, for generic parameters $\gamma, h > 0$.

Apart from the reversing symmetry $\mathbf{S}$, the reversing symmetry $(\mathbf{F} + \mathbf{G})\mathbf{S}$ may lead to additional symmetric orbit that form the intersections of its fixed set with W^u (W^s). Orbits arising from reversing symmetries $(\mathbf{F} + \mathbf{G})^{m_1}\mathbf{S}(\mathbf{F} + \mathbf{G})^{m_2}$, $m_1, m_2 \in \mathbb{Z}$ are equivalent to the ones considered above after relabeling n.

As already mentioned, if there are nonsymmetric orbits they occur in pairs, $\mathbf{z}_n$ and $\mathbf{S}\mathbf{z}_n$, due to the reversing symmetry (43). These orbits can be distinguished according to whether in the continuum limit they become degenerate forming a single solution or they remain two distinct genuine

solutions related by symmetry. For the analytical solutions (36) it is easily seen that those fall in the first class since each of them has a counterpart that is found by reversing the sign of the free parameter τ. In the limit $\Delta \to 0$ this parameter tends to zero and the pair of solutions coincides. Similar things may be expected in the case of multihump solutions, where analytical forms are not available. Genuinely nonsymmetric orbits, on the other hand, which remain so after taking the continuum limit, are found only on the line $\gamma = 0$. Here they appear in addition to symmetric solutions and have a symmetric real and an antisymmetric imaginary part. They can be explained by the symmetry of complex conjugation, which, in the case of no damping, leaves the DNLS invariant. Complex conjugation produces a pair of orbits $\mathbf{z}_n$ and $\mathbf{S}\mathbf{z}_n$ corresponding to ϕ_n and ϕ_n^*, respectively. For parameter values $\gamma > 0$, however, this symmetry is destroyed. In agreement with this result, no such orbits are found with the shooting algorithm for $\gamma > 0$ if the reference sphere is chosen sufficiently small.

C. A survey of multibreathers

In the following we present an illustration of the rich structure of multihump solutions exhibited by our DNLS system. In Fig. 8 we have scanned a large part of the existence domain for multihump structures, restricting ourselves to solutions localized within an overall bandwidth $|n| \leq 75$. If this interval is to be increased, one finds in addition broader multihump solutions with in principle an unlimited number of humps. The solutions are labeled by a 4-digit code
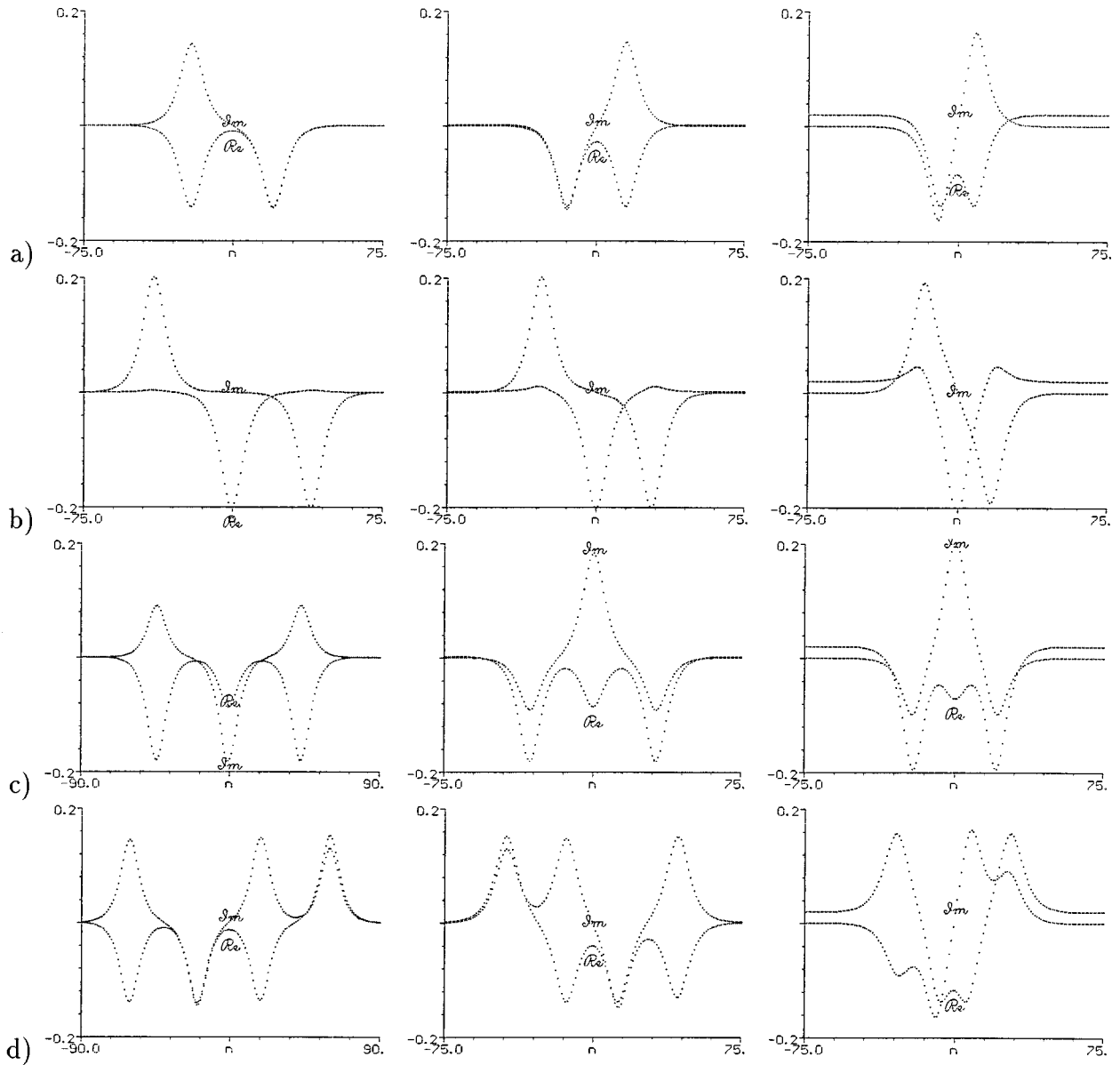
FIG. 9. Modulus $|\phi_n|$ of multibreathers localized within $|n| \leq 75$ for $\Gamma = 0$. Columns correspond to $H = 0.001$ (left), $H = 0.01$ (center), $H = 0.1$ (right). 4-digit labeling as explained in Sect. IV C: (a) 0211, (b) 2111, (c) 0321, and 0312, (d) 2222. Nonuniform labeling of the imaginary part is due to complex conjugation symmetry. $\Delta = 0.2$.

$n_1 n_2 n_3 n_4$ where n_1 and n_2 denote the number of maxima and minima of the real part, n_3 and n_4 the number of maxima and minima of the imaginary part. It proves sufficient for the labeling to count only maxima lying above and minima lying below the flat background, as we will do throughout this subsection.

Focusing on $\gamma = 0$ one sees that this line gives rise to many more structures than the rest of the existence region. This is not caused by multiplicities due to the complex conjugation symmetry (because symmetry pairs are only listed once here), but rather due to the fact that most solutions appear for infinitely small values h. In Fig. 9, a number of individual structures found for $\gamma = 0$ are shown for three values of driving h corresponding to $H = 0.001, 0.01, 0.1$. In the left column, corresponding to the near-integrable case $h \rightarrow 0$, solutions appear as compounds of weakly overlapping isolated humps, which, however, are not always identical to $\phi^\pm$. Towards the right of the figure we increased the driving

strength, thereby keeping track of the multihump solutions. Note in Fig. 9(a) that $\mathrm{Re}(\phi_n)$ taken at the center site $n = 0$ deviates from the flat background in the same measure as the driving is increased. Similar events are seen in Figs. 9(c) and 9(d) at other lattice sites that are located between two well defined single humps and where $\mathrm{Re}(\phi_n)$-$\mathrm{Re}(\phi_\infty)$ increases in absolute size with h. Viewing multibreathers as being generated by homoclinic orbits, it is reasonable to consider the largest of these deviations from the flat background as an estimate for the size of the chaotic region (homoclinic tangle) located around the hyperbolic fixed point.

For $\gamma > 0$ in the rest of the survey diagram of Fig. 8, contrarily to the effectively two dimensional case $\gamma = 0$, solutions appear and disappear as the driving is increased beyond certain values of h that in some cases do not coincide with the lower and the upper boundaries of the existence domain. A complete picture of the solutions found for $\Gamma = 0.3$ and localized within $|n| \leq 150$ is given in Fig. 10 to-
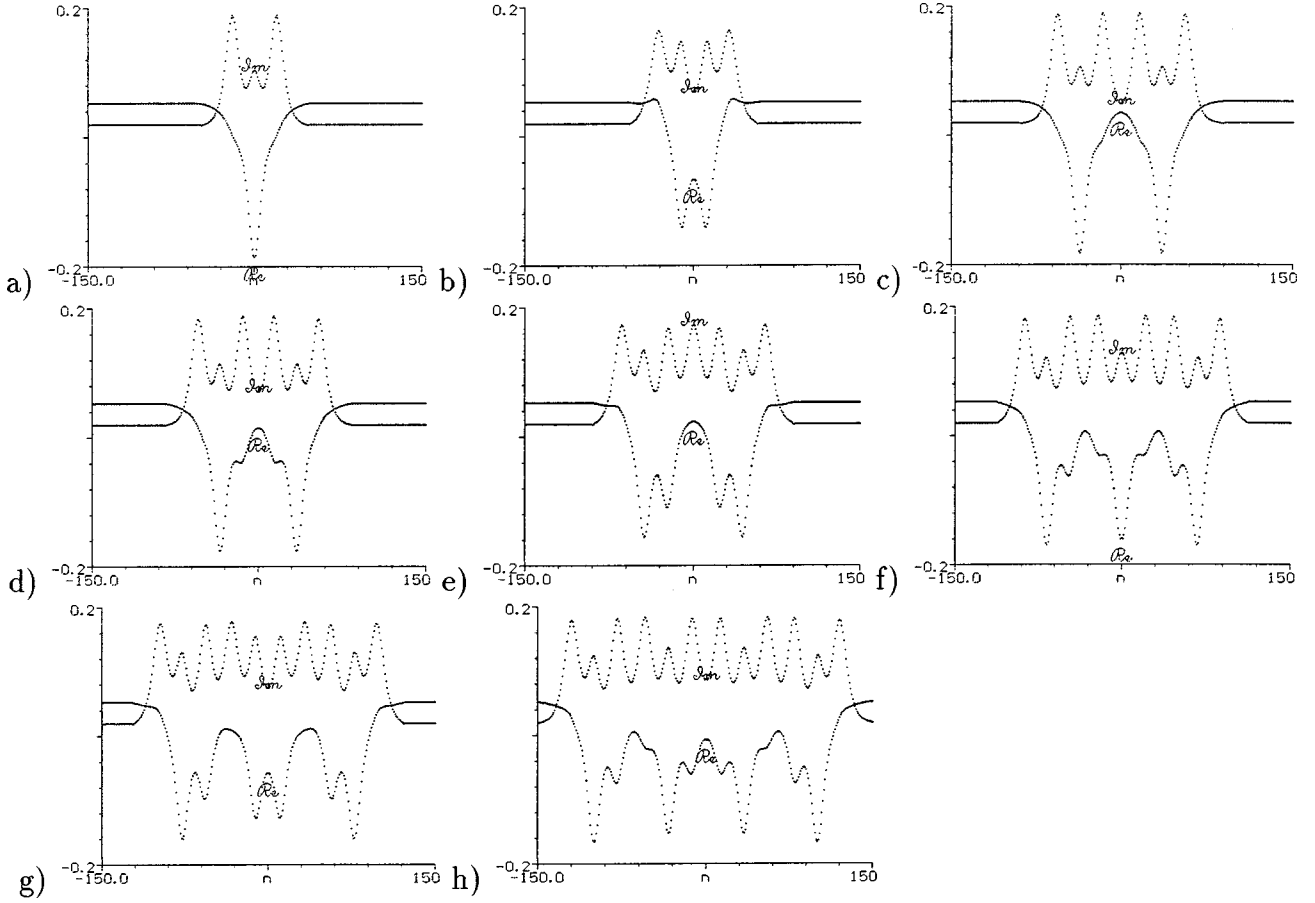
FIG. 10. Modulus $|\phi_n|$ of multibreathers found localized within $|n| \leq 150$ for $\Gamma = 0.3$ and $H = 0.25$. Labeling: (a) 2130, (b) 2240, (c) 0260, (d) 0460, (e) 0470, (f) 0790, (g) 06(10)0, (h) 08(12)0. $\Delta = 0.2$.

gether with the 4-digit code as explained above for the various solutions. The fact that some structures with a large number of extrema are missing in Fig. 8 is due to the restriction to smaller lattice sites $|n| \leq 75$.

The emergence and disappearance of multihump structures as functions of the driving amplitude can be better understood using an order parameter as a measure of complexity. While typically any bounded smooth functional of ϕ_n suits this purpose, we choose for the sum of the squared distances between orbit points and the fixed point in the complex ϕ_n plane, shortly called the breather's ''area''

$$A = \Delta \sum_{n=-\infty}^{\infty} |\phi_n - \phi_\infty|^2. \qquad (45)$$

Calculating A numerically as a function of h, we expect to detect global bifurcations at critical h values where the derivative of A diverges and which are associated with the appearance and disappearance of multibreathers.

In Fig. 11(a) this area order parameter is shown for the case $\gamma = 0$ with h varying over the existence interval $0 \leq h \leq h_+$. We observe the four multibreather solutions of lowest
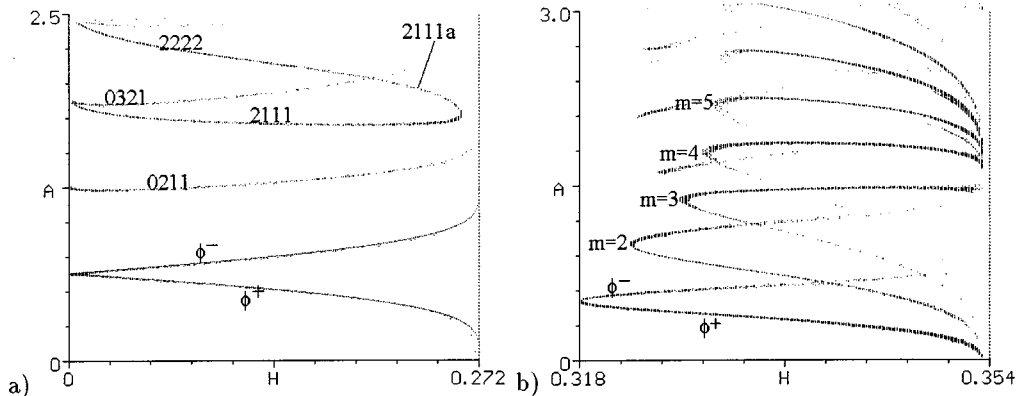

FIG. 11. Bifurcations of single- and multihumped solutions. Area (45) vs H in the interval $H_{\mathrm{thr}} \leq H \leq H_+$. (a) $\Gamma = 0$, (b) $\Gamma = 0.5$. Labeling as explained in Sect. IV C, $\Delta = 0.2$.

complexity, which were also seen in Fig. 9, plus the single humps ϕ^+, ϕ^- for which the area has been calculated from Eq. (36). Unfortunately, the shooting algorithm fails to capture some solutions in certain parts of the figure so we do not know their behavior as h approaches the upper bound. Nevertheless the picture is clear enough to draw some conclusions. Breather solutions are often, but not exclusively, born in pairs and cross the largest part of the existence domain with only a modest change of their area. Eventually they approach a point of more rapid change in area at a driving value that is smaller than or equal to h_+. Plotting the individual solution at this point one finds that they join smoothly with another solution. Two of these events are evident from our data. One of them, the bifurcation (flat solution, ϕ^+) at h_+ and $A=0$ was already stated in Sec. III A. The other bifurcation involving the pair $(2111,2111a)$ takes place at a driving value considerably away from the upper boundary. Here the multibreather $2111a$ has evolved from 2222 in a local bifurcation, corresponding to a change of labeling, which is not recognizable from the area plot of Fig. 11(a). One other global bifurcation involving the pair $(\phi^-, 0211)$ is less evident but may be conjectured to take place at or very close to the upper boundary h_+. It is worth noting that no partner breather has been found at the point where the structure 0211 is born except from its symmetry related complex conjugated version, and that the crossing of 0321 and 2222 is accidental, i.e., not related to a close approach of these two solutions in function space.

As a striking feature of the order parameter analysis, in the case $\gamma=0$ the lower threshold is equal for all breathers. This is again a consequence of the quasi-two-dimensionality of the DNLS system in this case. Namely, it can be qualitatively understood that multibreathers arise from intersections of the invariant manifolds of the double-hyperbolic fixed point. The geometry of these intersections takes place in a similar way as sketched in Sec. II for single hump solutions, the difference being that single hump structures are formed by intersections of the primary lobes of the manifolds whereas multibreathers involve secondary, ternary, and other higher order lobes.

In 2D maps it follows from geometrical arguments that homoclinic tangency is a global phenomenon affecting all homoclinic points or none. Thus if the manifolds intersect tangentially at some parameter value, all homoclinic orbits are created simultaneously. This statement cannot be generalized to higher-dimensional maps. In fact, we find a counterexample investigating the threshold scenario in our DNLS system for the general case of finite damping $\gamma > 0$. The bifurcation diagram is shown in Fig. 11(b) for a damping constant γ corresponding to $\Gamma = 0.5$. Here only the single-hump pair $\phi^\pm$ emerges at h_{thr}. Besides that we observe a succession of global bifurcations involving pairs of symmetric m-hump structures with $m = 2, 3, \ldots$ all having their own lower threshold values that increase with m and the area A. In addition to the m pairs one finds in Fig. 11(b) other multibreathers whose bifurcation properties remain incomplete and do not allow us to draw firm conclusions in these cases.

V. CONCLUSIONS

Since the spatial discretization of a pde on the infinite line is an unavoidable step in most numerical integration

schemes, it is interesting to ask what happens to the solutions of the pde and their basic properties upon such a discretization. In the case of the NLS this question has attained particular significance, in view of its many applications to optics, plasma physics and field theories in $1+1$ dimensions [4], as well as an increasing interest in the dynamical properties of nonlinear one-dimensional lattices [5].

Furthermore, if the discretized form of the NLS is a completely integrable, infinite-dimensional Hamiltonian system, as in the case of the Ablowitz-Ladik discretization adopted here, many analytical tools are available to study physically interesting perturbations of the NLS as well as the DNLS multi degree of freedom systems.

A particularly interesting class of solutions, which has attracted the attention of many researchers, are certain spatially localized structures called "solitons" by some due to their shape and properties in a moving frame of reference of the integrable limit, and "breathers" by others, in view of their periodic oscillations in time. The existence and stability of such structures in the case of a damped and periodically driven NLS was studied recently in a number of interesting papers by Barashenkov *et al.*

In this paper, we have studied these localized structures in a damped and driven DNLS system of the form (2). Our approach has been to substitute $\psi_n(t) = \phi_n \exp it$ in Eq. (2) and construct the stationary solutions ϕ_n as orbits of a 4D symplectic map (6).

Our main result is the discovery of a rich variety of localized structures in the form of homoclinic orbits that are asymptotic to a hyperbolic fixed point along its 2D stable and 2D unstable invariant manifold. These structures are characterized by an apparently arbitrary number of extrema in the n variation of their real and imaginary parts, according to which they can be classified, taking also into account their symmetries.

More specifically, we have determined analytically, using Mel'nikov's theory, a threshold line in the γ, h plane above which the two simplest such structures are found to exist. As a particular feature of this perturbed DNLS we saw that the first component of the Mel'nikov vector vanishes identically. The second Mel'nikov component possesses two distinct almost straight node lines generated at the point of homoclinic tangency and associated with the pair of breather solutions $\psi_n^\pm$. This in return allows one to calculate the lower existence boundary $h_{\text{thr}}(\gamma)$ of these fundamental solutions. Expressing this threshold in the NLS parameters we conclude that the linear law $H_{\text{thr}} = 2\Gamma/\pi$ holds exactly in the continuous system far beyond the nearly integrable regime. The upper boundary h_+, h^* of the breathers' existence domain appears to be identical to the one for the NLS, apart from scaling.

Here a comment may be in order concerning a possible link between dynamical systems theory and statistical mechanics. The notion of phase transitions is usually reserved for the thermodynamical limit at which the range of correlations between the particles of a statistical ensemble gives rise to sudden changes of global behavior. In the stationary damped driven DNLS we also encounter a nonanalytic change of order at the boundaries of the existence region, since the portion of 4D phase volume filled by chaotic orbits is equal to zero outside and different from zero exactly

within the existence domain. This sudden change is here established via a fixed point stability analysis leading to the upper boundary, together with the Mel'nikov analysis leading to the lower boundary of the existence region. This is the reason why we refer to the boundaries of the existence domain as phase transitions, and to our Fig. 1 as a phase diagram.

Furthermore, since the DNLS breathers can be identified by the primary intersection of invariant manifolds along one-loop homoclinic orbits, our approach allows us to understand qualitatively the emergence of more and more complicated localized structures (multibreathers) occurring at the multi-loop homoclinic orbits of secondary and higher order intersections between the 2D manifolds in 4D space. Using the area associated with a multiloop homoclinic orbit as order parameter we discovered that distinct multibreather solutions can have different driving parameter thresholds. For $\gamma \neq 0$ these thresholds occur above the single-hump threshold and are also larger as compared to the thresholds of other, less complex, multihump solutions. Knowing an analytic integral for the case $\gamma = 0, h > 0$, we relate the coincidence of all threshold values observed in this case to particular restrictive features imposed on the intersections of invariant manifolds in 2D maps.

Thus homoclinic chaos around a hyperbolic fixed point of Eq. (6) implies the existence of multihump localized oscillatory states of Eq. (2) with in principle arbitrary complexity. Indeed, using an appropriate shooting algorithm, we have been able to construct a large number of multibreather solutions numerically, characterized by an increasing number of humps as h grows above the existence threshold of the single-humps $\psi^{\pm}$.

All these solutions, however (except for ψ^{-} over a well defined region in the γ, h plane) are found to be marginally stable or unstable when integrated numerically for sufficiently long times. Thus, our results may be used to describe in a systematic way the complex spatiotemporal dynamics of this system by identifying a large class of solutions that are not only unstable in time but are also characterized by extreme irregularity in their spatial structure.

ACKNOWLEDGMENTS

APPENDIX A

For the completely integrable mapping $\mathbf{F}$ the invariant manifolds are found by the following, not necessarily unique, parametrization technique. Consider for each of the two integrals $I_k(\mathbf{q}, \mathbf{p})$, $k = 1, 2$ in Eq. (10), the Hamilton's equations of motion

$$\dot{\mathbf{p}} = -\partial I_k / \partial \mathbf{q}, \quad \dot{\mathbf{q}} = \partial I_k / \partial \mathbf{p}. \quad \text{(A1)}$$

Here the dot denotes derivative with respect to some continuous time variable t and q_i, p_i assume the roles of canonically conjugate variables, $i = 1, 2$. Since the Hamiltonian I_k is conserved, the flow (A1) takes place on the one-dimensional manifold labeled by a fixed value of I_k. For instance, in the case of the action integral I_1 of Eq. (10) we get

$$\dot{\mathbf{p}} = -\partial / \partial \mathbf{q} I_1 = -2\mathbf{q}(1 + \mathbf{p}^2) + 2\mu \mathbf{p}, \quad \text{(A2a)}$$

$$\dot{\mathbf{q}} = \partial / \partial \mathbf{p} I_1 = 2\mathbf{p}(1 + \mathbf{q}^2) - 2\mu \mathbf{q}. \quad \text{(A2b)}$$

Next $\mathbf{p}$ is eliminated from the integral (10) against $\dot{\mathbf{q}}$ using Eq. (A2b). Imposing $I_1 = \text{const}$ one obtains

$$\dot{\mathbf{q}}^2 / 4 = \mu^2 \mathbf{q}^2 + (I_1 - 1 - \mathbf{q}^2)(1 + \mathbf{q}^2), \quad \text{(A3)}$$

which can be integrated. In particular, on the homoclinic connection ($I_1 = 1$) one finds $\mathbf{q}(\tau) \sim \pm \sinh w \, \text{sech}(2t \sinh w)$.

In a similar manner the angular integral I_2 gives rise to a flow with a time variable θ. But since the integrals I_k are in involution the two flows are commutative, which is accomplished by taking the product of both solutions

$$\mathbf{q}(\tau, \theta) = \pm \sinh w \, \text{sech}(2t \sinh w) \begin{pmatrix} \cos \theta \\ \sin \theta \end{pmatrix}. \quad \text{(A4)}$$

Using theorems of hyperbolic functions, in particular relation (27), one can specify t_n, θ_n such that Eq. (A4) satisfies the mapping $\mathbf{F}$,

$$t_n = \frac{nw + \tau}{2\tau \sinh w}, \quad \tau, \theta_n \in \mathbf{R}, \quad \text{(A5)}$$

The desired two-parameter family of mapping solutions is then

$$\hat{\mathbf{q}}_n(\tau, \theta) = \pm \sinh w \, \text{sech}(nw + r) \begin{pmatrix} \cos \theta \\ \sinh \theta \end{pmatrix},$$

$$w = \cosh^{-} \mu, \quad 0 \leq \tau < w. \quad \text{(A6)}$$

The times τ and θ of the interpolating flows of type (A1) are the variables of the Mel'nikov vector. For a more general treatment of interpolating Hamiltonian flows for mappings related to stationary solutions of integrable pde's see [27].

APPENDIX B

Here we determine the stability of the fixed points r_i, $i = 0 \cdots 3$ of mapping (9). It is shown in following Eq. (10) that the DNLS mapping is symplectic even for h, $\gamma \neq 0$. In 4D symplectic mappings the eigenvalues of the Jacobian appear in pairs $\lambda_1 \lambda_2 = \lambda_3 \lambda_4 = 1$, similar to the 2D area-preserving case. Consequently, fixed points may be purely elliptic (EE) with $|\lambda_k| = 1$, $k = 1 \ldots 4$, or purely hyperbolic (HH) with all λ_k off the unit circle, or of mixed type. In the latter case we discriminate EH points ($|\lambda_{1,2}| = 1, |\lambda_3| = 1/|\lambda_4| < 1$), and HE points vice versa [21]. Analyzing the Jacobian of Eq. (9) one sees that the way fixed points fall into these four categories depends only on their amplitude r_i and the damping constant γ, namely, through the signs of two discriminants

TABLE II. Signs of Eq. (B1) for fixed points r_0, r_1, r_2, r_3.

	r_0		r_1		r_2		r_3	
	f_+	f_-	f_+	f_-	f_+	f_-	f_+	f_-
$0 < \gamma < \delta/2$			+	+	+	−	−	−
$\delta/2 < \gamma < \delta/\sqrt{3}$			−	−	+	−	−	−
$\delta/\sqrt{3} < \gamma$	−	−						

$$f_\pm(r) = (\mu - r)^2 \pm 2(\mu - r)\sqrt{r^2 - \gamma^2} - 2r - \gamma^2 - 1 \qquad (B1)$$

evaluated at $r = r_i$. Since the functions $f_\pm(r)$ have roots at the extrema (18), their signs are definite at every fixed point. They are displayed in Table II. Knowing the signs of ($r - \gamma$) and Eq. (B1), stability then follows according to Table III. Now we consider each fixed point separately:

Fixed point r_0: The polynomial (16) increases monotonically whence $P(r = \gamma) > (<) 0$ for $h < (>) h^*$. Hence for drivings below h^* we have $r_0 < \gamma$ and the fixed point r_0 is HH. For $h > h^*$ it follows from $r_0 > \gamma$ and the signs of Eq. (B1) that r_0 is EE. This fixed point changes quality again for ultrastrong drivings exceeding the value

$$h_{++}(\gamma) = 2\sqrt{2 + \delta} + \frac{5}{4\sqrt{2}} \gamma^2 + O(\gamma^2 \delta) > 2.82. \qquad (B2)$$

In this case r_0 is of mixed type (EH) because the discriminant f_- changes sign again at $r_{++} = \sqrt{\gamma^2 + (\delta + 2)^2} > 2$.

Fixed point r_3: We notice that r_- is an upper bound for γ; cf. Eq. (18). Hence $r_3 > \gamma$. It then follows from the signs of Eq. (B1) that r_3 is EE. For drivings larger than Eq. (B2) it eventually turns EH for the same reason as the fixed point r_0 does.

Fixed point r_2: Utilizing that $\gamma \leq r_- \leq r_2$ and Tables II and III it follows that r_2 is always HE. It exists for $h_- < h < h_+$.

Fixed point r_1: We consider first the case $h < h^*$. As $P(\gamma) > 0$ and $\gamma < r_- < r_2, r_3$ we have $\gamma > r_1$, and hence r_1 HH. Second, we consider strong driving $h > h^*$. It follows from $P(\gamma) < 0$ and the upper bound r_- for γ that $\gamma < r_1$. Again we conclude the stability from Tables II and III. However, here we encounter a phase transition at the critical point $\gamma = \delta/2$. Below this point the signs of both discriminants (B1) are positive, and r_1 is HH. Above the critical point both signs are negative implying r_1 EE. Note that the latter case includes two different scenarios: For $\delta/2 < \gamma < \frac{4}{7}\delta$ there are three fixed points, whereas for $\frac{4}{7}\delta < \gamma < \delta/\sqrt{3}$ and $h^* < h < h_-$ the point r_0 is the only fixed point.

TABLE III. Stability types as functions of the fixed point amplitude r. Labeling of eigenvectors: E for elliptic, H for hyperbolic.

$r < \gamma$		$r > \gamma$	
		$f_+(r) < 0$	$f_+(r) > 0$
HH	$f_-(r) < 0$	EE	HE
	$f_-(r) > 0$	EH	HH

APPENDIX C

The exact one-hump solutions (36) for $\gamma = 0$ are found as follows: The desired solutions will asymptotically tend to the smallest fixed point with modulus $\sqrt{r}$. This leads to the ansatz

$$\phi_n^\pm = \sqrt{r}(1 + 2\alpha \xi_n^{-1}). \qquad (C1)$$

Assuming the solutions to be real, the fixed point equation (16) for r reduces to $h = \sqrt{r}(\delta - r)$. Substituting h and Eq. (C1) in Eq. (6) we get a mapping in ξ_n

$$\frac{\xi_{n+1} + \xi_{n-1}}{\xi_{n+1} \xi_{n-1}} [\xi_n^2 + r(2\alpha + \xi_n)^2] = 2[\mu \xi_n - 2r(\alpha + \xi_n)]. \qquad (C2)$$

In the limit $\Delta \to 0$, Eq. (C1) have to yield the NLS dark and bright solitons. This implies a solution of the form $\xi_n = 1 \pm \beta \cosh(nB + \tau)$ with β, τ, B to be determined. Using addition theorems for the hyperbolic functions, the nearest-neighbor terms in the previous equation are

$$\xi_{n+1} + \xi_{n-1} = 2 + 2\beta\kappa x, \qquad (C3a)$$

$$\xi_{n+1}\xi_{n-1} = 1 + 2\beta\kappa x + \beta^2(\sinh^2 B + x^2) \qquad (C3b)$$

with $\kappa = \cosh B$ and $x = \cosh(nB + \tau)$.

Next, we insert Eq. (C3) in Eq. (C2) and order in powers of x. Since the ξ_n mapping holds at all lattice sites n we may equate coefficients of equal powers. With the highest term being cubic this gives four equations. The cubic and quadratic equations are solved as

$$r = \frac{\mu - \kappa}{2 + \kappa}, \quad \kappa = 1 + \frac{2\alpha\delta}{2\alpha + 3 + \delta} \qquad (C4)$$

or, eliminating κ,

$$r = \frac{\delta}{3 + 2\alpha}. \qquad (C5)$$

The remaining equations involve only α, β and are consistently solved by

$$4\alpha = (\delta + 2)(\beta^2 - 1) - 3$$
$$\pm \sqrt{(1 + 2\beta^2)^2 + 2\delta(1 - 3\beta^2 + 2\beta^4) + \delta^2(1 - \beta^2)^2}, \qquad (C6)$$

$$\beta^2 = 1 + \alpha \frac{2\alpha + 3}{2\alpha + 3 + \delta(\alpha + 1)}. \qquad (C7)$$

As argued below only the positive root can occur in Eq. (C6). With $\beta^2 = b$, $\alpha = a$ this leads to the family of solutions (36). For the purpose of numerics one determines the coefficients in the order r, κ, α, β.

In the continuum limit, letting $\delta \to 0$ one sees that in Eq. (C6) only the positive square root can occur, a case in which α, β reduce to hyperbolic functions in agreement with Eq. (C7). However, in order to satisfy Eq. (C4) we need $\alpha = \beta^2 - 1 \to \pm\infty$. This gives the continuum dark and bright solitons.

In the integrable limit r vanishes but not δ. From Eq. (C4) we see that then $\kappa = \mu$ and $\alpha, \beta = \pm\infty$. It is slightly harder to show that this results indeed in the integrable solution (13). Hereto we write out the general solutions (36) with α eliminated in favor of β, and evaluate in the limit $\beta \rightarrow \infty$:

$$\phi_n^{\pm} = \sqrt{r}\left(1 + \frac{(\beta^2 - 1)(1 + \mu)}{1 \pm \beta \cosh(\tau + n \cosh^{-1} \mu)}\right)$$

$$\rightarrow \pm \sqrt{r}\beta(1 + \mu)\operatorname{sech}(nw + \tau). \tag{C8}$$

It remains to show that the prefactor of the sech function is equal to sinh w. We can eliminate κ in Eq. (C4), solve for r and using Eq. (C7) express the prefactor for $\alpha \rightarrow \infty$ as

$$\sqrt{r}\beta(1 + \mu) = \left(\frac{\delta}{3 + 2\alpha}\right)^{1/2}\left(1 + \frac{2\alpha}{2 + \delta}\right)^{1/2}(1 + \mu)$$

$$= \left(\frac{\delta}{1 + \mu}\right)^{1/2}(1 + \mu) = \sqrt{(\mu - 1)(1 + \mu)}$$

$$= \sqrt{\mu^2 - 1} = \sinh w. \tag{C9}$$

[1] D. J. Kaup and A. C. Newell, Phys. Rev. B **18**, 5162 (1978); J. C. Eilbeck, P. S. Lomdahl, and A. C. Newell, Phys. Lett. **87A**, 1 (1981); P. S. Lomdahl, O. H. Soerensen, and P. L. Christiansen, Phys. Rev. B **25**, 5737 (1982); P. S. Lomdahl and M. R. Samuelson, Phys. Rev. A **34**, 664 (1986); G. Wysin and A. R. Bishop, J. Magn. Magn. Mater. **54-57**, 1132 (1986); A. M. Kosevich, B. A. Ivanov, and A. S. Kovalev, Phys. Rep. **194**, 118 (1990).

[2] K. Nozaki and N. Bekki, Phys. Rev. Lett. **50**, 1226 (1983); Phys. Lett. **102A**, 383 (1984); J. Phys. Soc. Jpn. **54**, 2363 (1985); Physica D **21**, 381 (1986).

[3] L. A. Lugiato and R. Lefever, Phys. Rev. Lett. **58**, 2209 (1987); M. Haeltermann, S. Trillo, and S. Wabnitz, Opt. Lett. **17**, 745 (1992); Opt. Commun. **91**, 401 (1992).

[4] *The Nonlinear Schrödinger Equation*, special issue of Physica D **87**, 201 (1995), Chap. 3

[5] L. M. Floría, J. L. Marín, S. Aubry, P. J. Martínez, F. Falo, and J. J. Mazo, Physica D **113**, 387 (1998).

[6] D. J. Kaup and A. C. Newell, Proc. R. Soc. London, Ser. A **361**, 413 (1978).

[7] I. V. Barashenkov and Yu. S. Smirnov, Phys. Rev. E **54**, 5707 (1996).

[8] I. V. Barashenkov and Yu. S. Smirnov, Phys. Rev. E **57**, 2350 (1997).

[9] B. A. Malomed, Phys. Rev. A **44**, 6954 (1991); Phys. Rev. E **47**, 2874 (1993).

[10] D. Cai, A. R. Bishop, N. Grønbech-Jensen, and B. A. Malomed, Phys. Rev. E **49**, 1677 (1994).

[11] S. Wabnitz, Opt. Lett. **18**, 601 (1993).

[12] J. L. Marín and S. Aubry, Nonlinearity **9**, 1501 (1996); S. Aubry, Physica D **103**, 201 (1997).

[13] R. S. MacKay and S. Aubry, Nonlinearity **7**, 1623 (1994); R. S. MacKay, Physica D **86**, 122 (1995); S. Aubry, *ibid.* **86**, 284 (1995).

[14] D. Hennig, K. Ö. Rasmussen, H. Gabriel, and A. Bülow, Phys. Rev. E **54**, 5788 (1996).

[15] T. Bountis, A. Goriely, and M. Kollmann, Phys. Lett. A **206**, 38 (1995).

[16] M. Kollmann and T. Bountis, Physica D **113**, 397 (1998).

[17] M. Ablowitz and J. Ladik, J. Math. Phys. **16**, 598 (1975); **17**, 1011 (1976).

[18] I. V. Barashenkov, M. M. Bogdan, and T. Zhanlav, in *Proceedings of the Fourth International Workshop on Nonlinear and Turbulent Processes in Physics, Kiew, 1989*, edited by V. G. Bar'yakhtar (World Scientific, Singapore, 1990), p. 3.

[19] G. Terrones, D. W. McLaughlin, E. A. Overman, and A. J. Pearlstein, SIAM (Soc. Ind. Appl. Math.) J. Appl. Math. **50**, 791 (1990).

[20] M. L. Glasser, V. G. Papageorgiou, and T. C. Bountis, SIAM (Soc. Ind. Appl. Math.) J. Appl. Math. **49**, 692 (1989).

[21] See, e.g., R. S. MacKay and J. Meiss, *Hamiltonian Dynamical Systems* (Adam Hilger, Bristol, 1986).

[22] K. H. Spatschek, H. Pietsch, E. W. Laedke, and Th. Eickermann, in *Singular Behaviour and Nonlinear Dynamics*, edited by T. Bountis and St. Pnevmatikos (World Scientific, Singapore, 1989).

[23] *Surveys in Applied Mathematics, Volume 1*, edited by J. P. Keller, D. W. McLaughlin, and G. C. Papanicolaou (Plenum Press, New York, 1995).

[24] A. B. Aceves, C. De Angelis, G. G. Luther, A. M. Rubenchik, and S. T. Turitsyn, Physica D **87**, 262 (1995).

[25] W. van Saarloos and P. C. Hohenberg, Phys. Rev. Lett. **64**, 749 (1990); Physica D **56**, 303 (1992); R. Alvarez, M. van Hecke, and W. van Saarloos, Phys. Rev. E **56**, R1306 (1997).

[26] J. Lamb and J. A. G. Roberts, Physica D **112**, 1 (1998).

[27] M. Bruschi, O. Ragnisco, P. M. Santini, and T. Gui-Zhang, Physica D **49**, 273 (1991).